Petroleum Science 23 (2026) 626–642

Contents lists available at ScienceDirect

Petroleum Science

journal homepage: www.keaipublishing.com/en/journals/petroleum-science

Original Paper

Seismic simulation for distributed acoustic sensing data using a novel stress and strain-rate elastic wave equation

Chong Zhao [a], Ji-Dong Yang [a,*], Jian-Ping Huang [a], Ning Qin [b], Kun Tian [b], Fei-Long Yang [c]

[a] State Key Laboratory of Deep Oil and Gas, Geosciences Department, China University of Petroleum (East China), Qingdao, 266580, Shandong, China
[b] Geophysical Research Institute, Shengli Oilfield Branch Co., SINOPEC, Dongying, 257022, Shandong, China
[c] School of Earth Sciences and Engineering, Xi'an Shiyou University, Xi'an, 710065, Shaanxi, China

ARTICLE INFO

Article history:
Received 13 May 2025
Received in revised form
17 July 2025
Accepted 8 September 2025
Available online 15 September 2025

Edited by Meng-Jiao Zhou

Keywords:
DAS simulation
First-order stress and strain-rate elastic wave equation
Normal strain-rate wavefields
Helical-wound optical fiber

ABSTRACT

Distributed acoustic sensing (DAS) is an advanced seismic acquisition technology with many advantages, such as low cost, wide frequency band, dense spatial sampling, and continuous recording. The straight optical fiber is restricted to single-component data and exhibits the lack of broadside sensitivity. To address the limitations of straight optical fiber and investigate the seismic response of multi-component DAS system, we proposed a novel first-order stress and strain-rate elastic wave equation to simulate the propagation of strain-rate wavefields. Compared to conventional particle-velocity wavefields, the simulations of three numerical examples demonstrate that the proposed equation can correctly generate elastic normal strain-rate wavefields and produce multi-component DAS data. Additionally, the simulations indicate that increasing the gauge length reduces the measurement accuracy of DAS, and a helical-wound optical fiber at a winding angle of 35.3° remains insensitive to S-wave, whereas it can clearly record S-wave at 54.7°. Furthermore, this equation can be directly implemented for multi-component DAS revers time migration (RTM) or FWI, thereby eliminating the need for traditional data conversion.

1. Introduction

Distributed acoustic sensing (DAS) is a developed seismic acquisition technology which has been gradually applied in both academic experiments and industrial production. It presents a variety of advantages over traditional geophone, including low cost, broad frequency coverage, dense spatial sampling, resistance to high temperatures and pressures, and long-term continuous monitoring (Li et al., 2022; Willis and Mark, 2022; Kislov et al., 2022).

DAS measures seismic strain or strain-rate along the fiber by detecting the phase changes in Rayleigh backscattered waves (Posey et al., 2000; Masoudi et al., 2013). Currently, straight optical fiber has been extensively employed in vertical seismic profiling (VSP) for high-resolution reservoir imaging (Mateeva et al., 2013; Madsen et al., 2013; Hall et al., 2019), microseismic monitoring (Stork et al., 2020; Staněk et al., 2022), time-lapse seismic monitoring (Dou et al., 2016; Harris et al., 2016; Byerley et al., 2018), and near-surface exploration (Dou et al., 2017; Bakulin et al., 2017, 2020). Despite those advantages, DAS using straight optical fiber is subject to certain inherent limitations. A major issue is the lack of broadside sensitivity, which means straight optical fiber insensitive to the normally incident seismic waves, resulting in weak signals at near-offset (Kuvshinov, 2016). However, the near-offset data is crucial for enhancing vertical-resolution of seismic imaging. Consequently, the straight optical fiber is not conducive to improve vertical-resolution of seismic imaging.

To address the broadside insensitivity of straight optical fiber, the helical-wound optical fiber has been proposed and applied in field trials (Lumens et al., 2013; Hornman, 2017; Hendi et al., 2020). By altering the geometry, helical-wound optical fiber allows for sampling in multiple tangential directions, thereby producing the multi-component strain or strain-rate data. Ning and Sava (2018a, 2018b) designed a multi-fiber configuration to obtain the strain tensor, and further achieved seismic imaging. Eaid et al. (2020) combined multi-

* Corresponding author.
E-mail address: jidong.yang@upc.edu.cn (J.-D. Yang).
Peer review under the responsibility of China University of Petroleum (Beijing).

https://doi.org/10.1016/j.petsci.2025.09.015

component seismic data from traditional geophones and helical-wound optical fibers to implement multi-parameter elastic full-waveform inversion (FWI) and analyzed the wavefield sensitivity to different fiber geometries. Zhang et al. (2024) developed an irregular configuration for helical-wound optical fibers to obtain the multi-component seismic strain, which was subsequently utilized in elastic RTM with a P/S separation strategy.

Seismic simulation can optimize the DAS geometry and subsequent data processing. The modeling of straight optical fiber has significantly advanced. For instance, Ma et al. (2020) successfully modeled the z-component strain wavefields in VSP based on the traditional stress-velocity equation. Shi et al. (2024) designed three DAS geometries and simulated the axial strain-rate wavefields of straight optical fibers. Celli et al. (2024) used numerical simulation to quantitatively analyze the impact of instrument coupling on DAS measurement. Additionally, the advent of helical-wound optical fiber has further developed the multi-component DAS technology. Such as Innanen et al. (2017) formulated the tangent vector and simulated the strain tensor for both arbitrary and nested helix geometries. Ning and Sava (2018a) introduced a multi-component DAS system utilizing helical-wound optical fiber to obtain the strain tensor in elastic media. Eaid et al. (2018) designed a complex-shaped optical fiber and performed elastic stress-velocity wave equation to achieve multi-component strain wavefields. Ning and Sava (2018b) developed a geometry consisting of five equally spaced helical-wound optical fibers and one straight optical fiber to acquire six different strain projections, and successfully constructing all components of strain tensor.

Previous studies on simulation of DAS typically begin with solving the traditional stress-velocity wave equation, followed by converting the displacement or particle-velocity into strain or strain-rate. This strategy involves data conversion and cannot directly obtain DAS data. Moreover, data conversion introduces certain errors, which can further damage the results of DAS seismic imaging or FWI. In this study, we present a novel stress and strain-rate elastic wave equation that can produce normal strain-rate wavefields, allowing for DAS RTM or FWI without data conversion. Based on the traditional first-order stress-velocity elastic wave equation and the stress-displacement relationship, we first derive the first-order stress and strain-rate elastic wave equation. Subsequently, this equation is solved using a staggered-grid finite-difference method with a CPML boundary condition and the CFL stability condition to generate the normal strain-rate wavefields. Furthermore, we evaluate the impact of gauge length on DAS and analyze the seismic response of helical-wound optical fibers at winding angles of 35.3° and 54.7°

The rest of this work is organized as follows: First, we derive the first-order stress and strain-rate elastic wave equation. Then, the seismic response of helical-wound optical fibers at winding angles of 35.3° and 54.7° are calculated. Next, we evaluate the impact of gauge length on the DAS by averaging the strain-rate wavefields over multi grids. Finally, three 2D numerical examples are used to demonstrate the numerical accuracy and stability of the proposed novel equation.

2. Theory

2.1. The elastic wave equation with stress and strain-rate components

In the isotropic media, the conventional 3D elastic wave equation can be written in terms of velocities and stresses as follows (Virieux, 1986):

$$
\begin{aligned}
\rho\frac{\partial v_x}{\partial t} &= \frac{\partial \sigma_{xx}}{\partial x}+\frac{\partial \sigma_{xy}}{\partial y}+\frac{\partial \sigma_{xz}}{\partial z},\\
\rho\frac{\partial v_y}{\partial t} &= \frac{\partial \sigma_{yx}}{\partial x}+\frac{\partial \sigma_{yy}}{\partial y}+\frac{\partial \sigma_{yz}}{\partial z},\\
\rho\frac{\partial v_z}{\partial t} &= \frac{\partial \sigma_{zx}}{\partial x}+\frac{\partial \sigma_{zy}}{\partial y}+\frac{\partial \sigma_{zz}}{\partial z},\\
\frac{\partial \sigma_{xx}}{\partial t} &= (\lambda+2\mu)\frac{\partial v_x}{\partial x}+\lambda\left(\frac{\partial v_y}{\partial y}+\frac{\partial v_z}{\partial z}\right),\\
\frac{\partial \sigma_{yy}}{\partial t} &= (\lambda+2\mu)\frac{\partial v_y}{\partial y}+\lambda\left(\frac{\partial v_x}{\partial x}+\frac{\partial v_z}{\partial z}\right),\\
\frac{\partial \sigma_{zz}}{\partial t} &= (\lambda+2\mu)\frac{\partial v_z}{\partial z}+\lambda\left(\frac{\partial v_x}{\partial x}+\frac{\partial v_y}{\partial y}\right),\\
\frac{\partial \sigma_{xy}}{\partial t} &= \mu\left(\frac{\partial v_x}{\partial y}+\frac{\partial v_y}{\partial x}\right),\\
\frac{\partial \sigma_{yz}}{\partial t} &= \mu\left(\frac{\partial v_y}{\partial z}+\frac{\partial v_z}{\partial y}\right),\\
\frac{\partial \sigma_{xz}}{\partial t} &= \mu\left(\frac{\partial v_x}{\partial z}+\frac{\partial v_z}{\partial x}\right),
\end{aligned}
\tag{1}
$$

where $\sigma_{ij}=(i,j=x,y,z)$ is stress, $v_i(i=x,y,z)$ is particle-velocity, λ and μ are the Lame parameters, ρ is density, and t is duration time. The stresses and displacements in elastic isotropic media satisfy

$$
\begin{aligned}
\sigma_{xx} &= (\lambda+2\mu)\frac{\partial u_x}{\partial x}+\lambda\left(\frac{\partial u_y}{\partial y}+\frac{\partial u_z}{\partial z}\right),\\
\sigma_{yy} &= (\lambda+2\mu)\frac{\partial u_y}{\partial y}+\lambda\left(\frac{\partial u_x}{\partial x}+\frac{\partial u_z}{\partial z}\right),\\
\sigma_{zz} &= (\lambda+2\mu)\frac{\partial u_z}{\partial z}+\lambda\left(\frac{\partial u_x}{\partial x}+\frac{\partial u_y}{\partial y}\right),\\
\sigma_{xy} &= \mu\left(\frac{\partial u_x}{\partial y}+\frac{\partial u_y}{\partial x}\right),\\
\sigma_{yz} &= \mu\left(\frac{\partial u_y}{\partial z}+\frac{\partial u_z}{\partial y}\right),\\
\sigma_{xz} &= \mu\left(\frac{\partial u_x}{\partial z}+\frac{\partial u_z}{\partial x}\right),
\end{aligned}
\tag{2}
$$

where $u_i(i=x,y,z)$ is displacement. Defining the normal strain-rate as $\dot{\varepsilon}_{ii}(i=x,y,z)$, which satisfies the following relationship with particle-velocity:

$$
\dot{\varepsilon}_{xx}=\frac{\partial v_x}{\partial x},\ \dot{\varepsilon}_{yy}=\frac{\partial v_y}{\partial y},\ \dot{\varepsilon}_{zz}=\frac{\partial v_z}{\partial z},
\tag{3}
$$

where $\dot{\varepsilon}_{xx}$, $\dot{\varepsilon}_{yy}$ and $\dot{\varepsilon}_{zz}$ are the normal strain-rate components in x, y, and z directions, respectively.

Taking $\dot{\varepsilon}_{xx}$ as an example, we can briefly outline the derivation of the novel equation. First, by multiplying both sides of Eq. (1) by $\frac{1}{\partial x}$, we obtain

$$
\rho\frac{\partial v_x}{\partial t\partial x}=\frac{\partial \sigma_{xx}}{\partial x\partial x}+\frac{\partial \sigma_{xy}}{\partial y\partial x}+\frac{\partial \sigma_{xz}}{\partial z\partial x}.
\tag{4}
$$

According to the Eqs. (2) and (3), Eq. (4) can be further rewritten as

$$\rho\frac{\partial\dot{\varepsilon}_{xx}}{\partial t}=\frac{\partial\left[(\lambda+2\mu)\frac{\partial u_x}{\partial x}+\lambda\left(\frac{\partial u_y}{\partial y}+\frac{\partial u_z}{\partial z}\right)\right]}{\partial x^2}+\frac{\partial\left[\mu\left(\frac{\partial u_x}{\partial y}+\frac{\partial u_y}{\partial x}\right)\right]}{\partial y\partial x}+\frac{\partial\left[\mu\left(\frac{\partial u_x}{\partial z}+\frac{\partial u_z}{\partial x}\right)\right]}{\partial z\partial x}. \tag{5}$$

Based on the relationship between strain and displacement, as well as the rules of differentiation, Eq. (5) can be rewritten as

$$\rho\frac{\partial\dot{\varepsilon}_{xx}}{\partial t}=\frac{\partial\left[(\lambda+2\mu)\varepsilon_{xx}+\lambda\left(\varepsilon_{yy}+\varepsilon_{zz}\right)\right]}{\partial x^2}+\frac{\partial(\mu\varepsilon_{xx})}{\partial y^2}+\frac{\partial\left(\mu\varepsilon_{yy}\right)}{\partial x^2}+\frac{\partial(\mu\varepsilon_{xx})}{\partial z^2}+\frac{\partial(\mu\varepsilon_{zz})}{\partial x^2}, \tag{6}$$

with

$$\begin{aligned}\sigma_{xx}&=(\lambda+2\mu)\varepsilon_{xx}+\lambda\left(\varepsilon_{yy}+\varepsilon_{zz}\right),\\ \tau_{xx}&=\mu\varepsilon_{xx},\\ \tau_{yy}&=\mu\varepsilon_{yy},\\ \tau_{zz}&=\mu\varepsilon_{zz},\end{aligned} \tag{7}$$

where the $\varepsilon_{ii}(i=x,y,z)$ is normal seismic strain, the $\tau_{ii}(i=x,y,z)$ is auxiliary variable, taking the time derivative of both sides of Eq. (7), the first-order equation of $\dot{\varepsilon}_{xx}$ can be derived as

$$\begin{aligned}\rho\frac{\partial\dot{\varepsilon}_{xx}}{\partial t}&=\frac{\partial^2\sigma_{xx}}{\partial x^2}+\frac{\partial^2\tau_{xx}}{\partial y^2}+\frac{\partial^2\tau_{yy}}{\partial x^2}+\frac{\partial^2\tau_{xx}}{\partial z^2}+\frac{\partial^2\tau_{zz}}{\partial x^2},\\ \frac{\partial\sigma_{xx}}{\partial t}&=(\lambda+2\mu)\dot{\varepsilon}_{xx}+\lambda\left(\dot{\varepsilon}_{yy}+\dot{\varepsilon}_{zz}\right),\\ \frac{\partial\tau_{xx}}{\partial t}&=\mu\dot{\varepsilon}_{xx},\\ \frac{\partial\tau_{yy}}{\partial t}&=\mu\dot{\varepsilon}_{yy},\\ \frac{\partial\tau_{zz}}{\partial t}&=\mu\dot{\varepsilon}_{zz},\end{aligned} \tag{8}$$

where the $\dot{\varepsilon}_{ii}(i=x,y,z)$ is normal strain-rate, $\sigma_{ii}=(i=x,y,z)$ is normal stress, $\tau_{ii}(i=x,y,z)$ is auxiliary variable.

Similarly, the first-order equations for $\dot{\varepsilon}_{yy}$ and $\dot{\varepsilon}_{zz}$ can also be derived. Here, we present the complete first-order stress and strain-rate elastic wave equation:

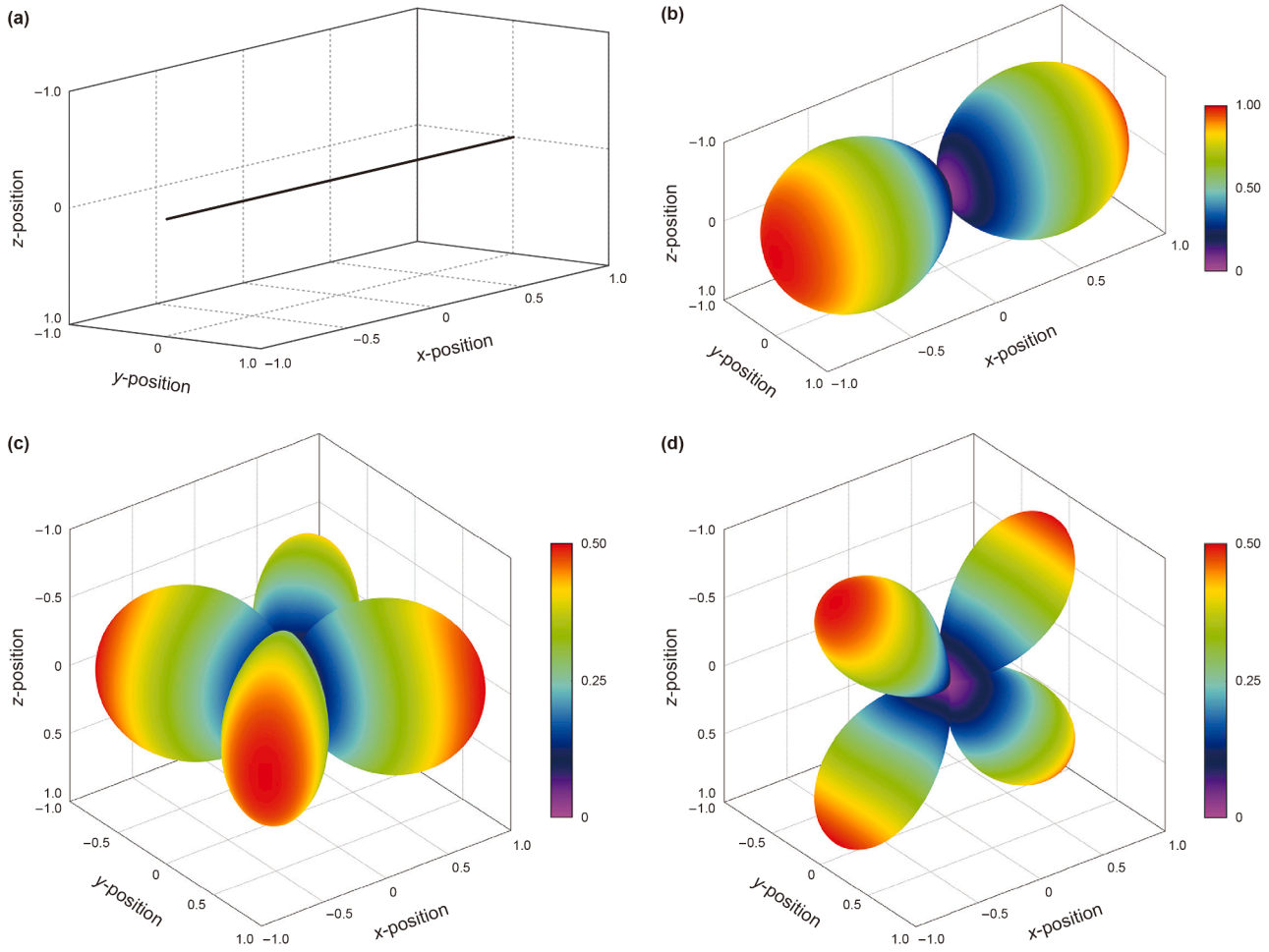

Fig. 1. The straight optical fiber and corresponding amplitude radiation patterns. Panel **(a)** shows straight optical fiber along *x*-direction. Panel **(b)** shows P-wave radiation pattern. Panel **(c)** shows SH-wave radiation pattern. Panel **(d)** shows SV-wave radiation pattern.

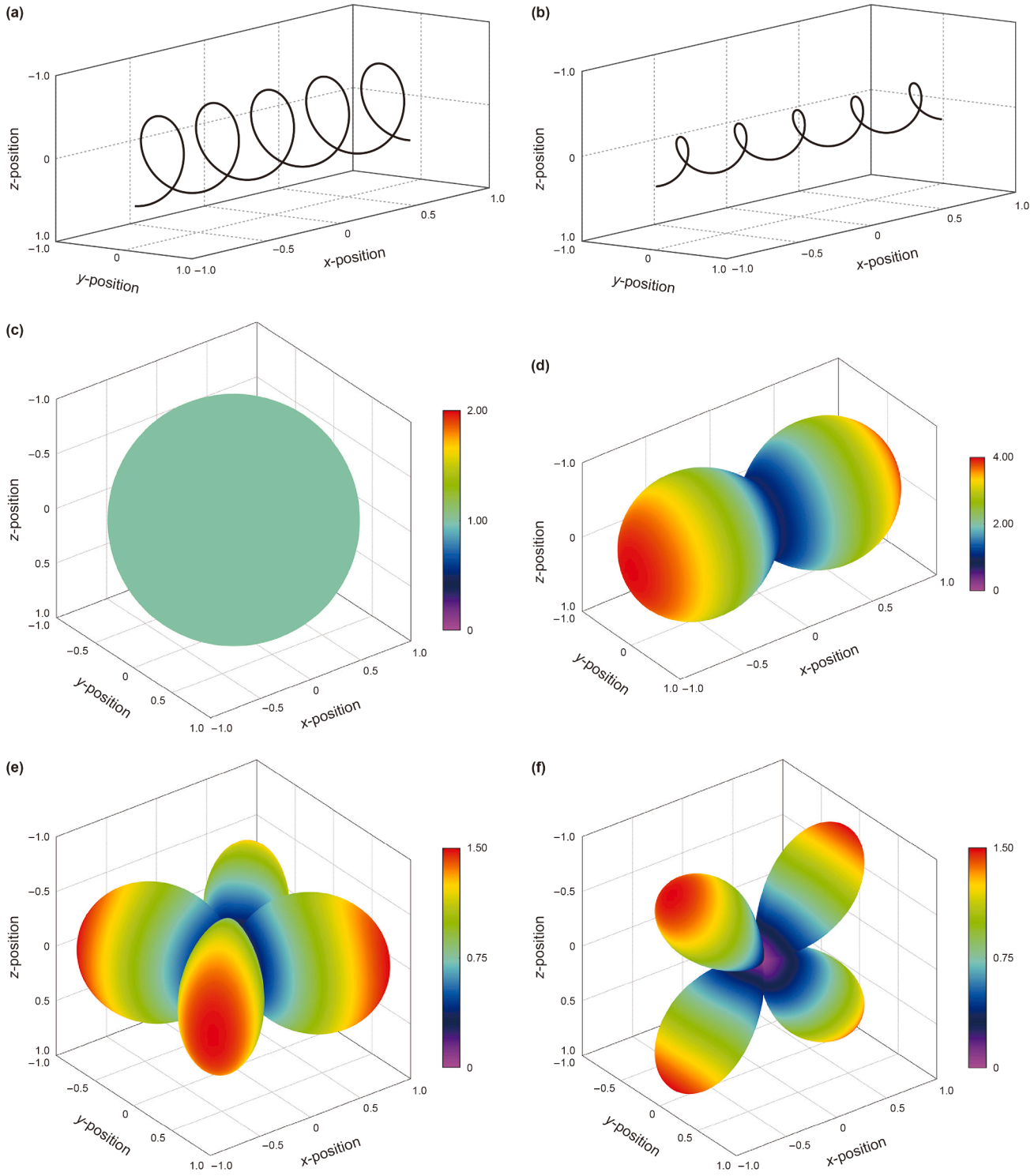

Fig. 2. The helical-wound optical fibers and corresponding amplitude radiation patterns. Panel **(a)** is 35.3° helical fiber along the *x*-direction. Panel **(b)** is 54.7° helical fiber along the *x*-direction. Panel **(c)** shows P-wave radiation pattern of 35.3° fiber. Panel **(d)** shows P-wave radiation pattern of 54.7° fiber. Panel **(e)** shows SH-wave radiation pattern of 54.7° fiber. Panel **(f)** shows SV-wave radiation pattern of 54.7° fiber.

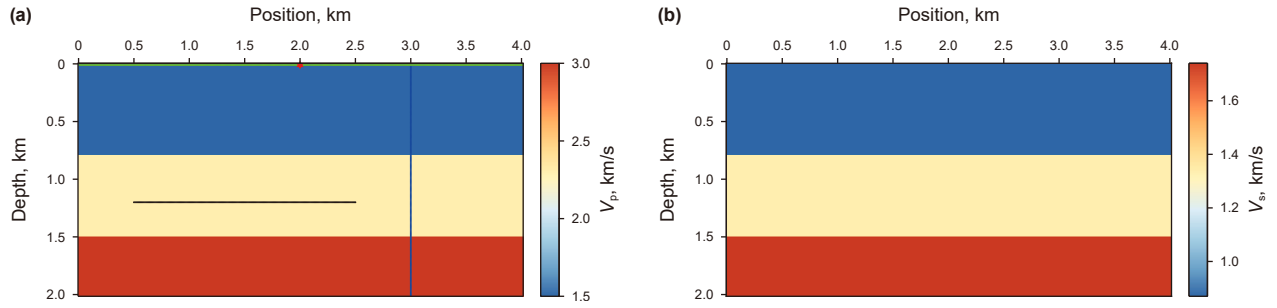

Fig. 3. The P- **(a)** and S-wave **(b)** velocities (V_p and V_s) for the layered model. The red star denotes the source location, green dots denote receivers on the surface, black dots denote receivers in a horizontal well, and blue dots denote receivers in a vertical well.

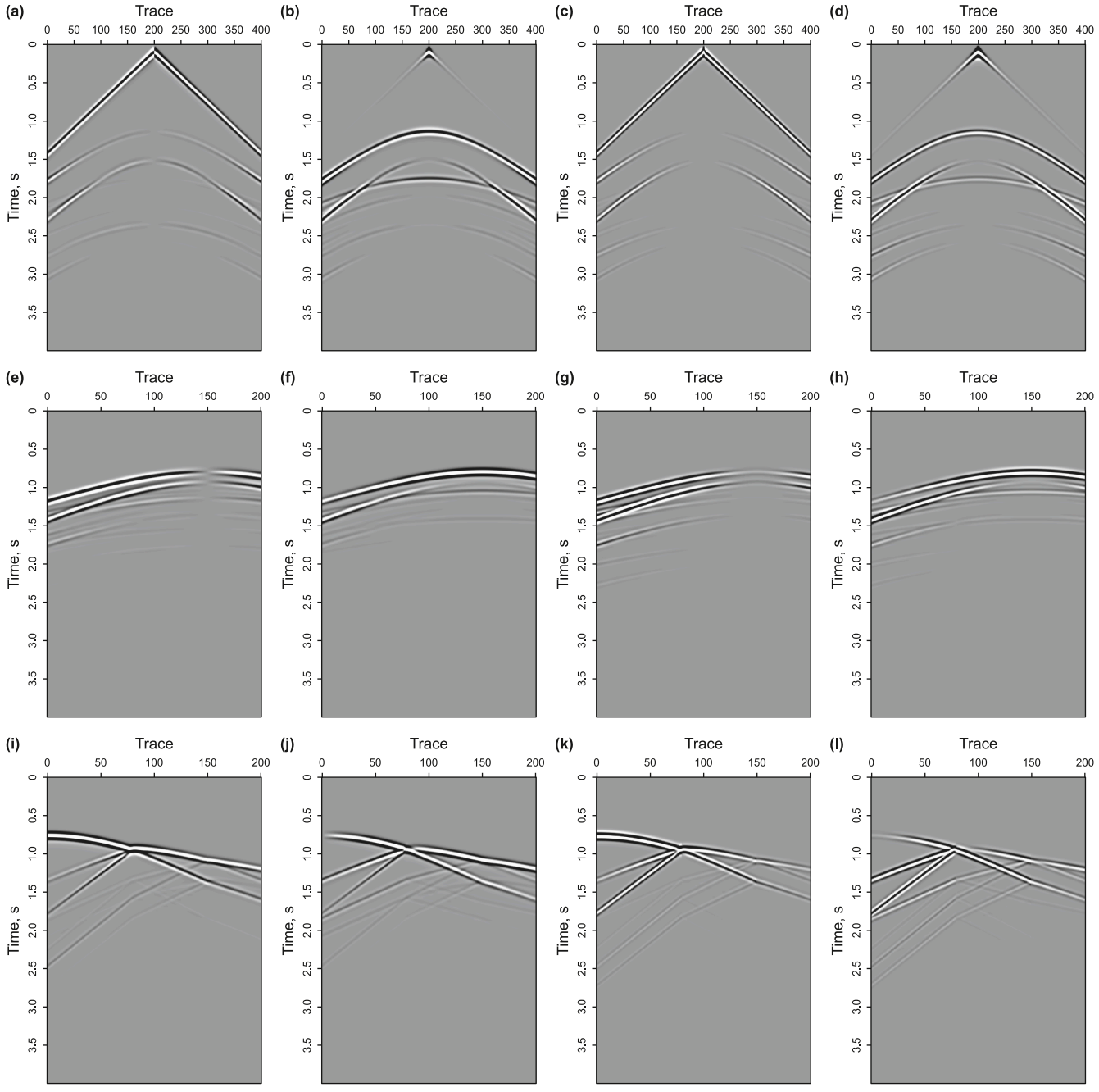

Fig. 4. Common-shot gathers for the layered model. The first row displays receivers on the surface, panels **(a)** and **(b)** show *x*- and *z*-component particle-velocity seismograms, and panels **(c)** and **(d)** show *x*- and *z*-component strain-rate seismograms. The second row displays receivers in the horizontal well, panels **(e)** and **(f)** show *x*- and *z*-component particle-velocity seismograms, panels **(g)** and **(h)** show *x*- and *z*-component strain-rate seismograms. The third row displays receivers in the vertical well, panels **(i)** and **(j)** show *x*- and *z*-component particle-velocity seismograms, and panels **(k)** and **(l)** show *x*- and *z*-component strain-rate seismograms.

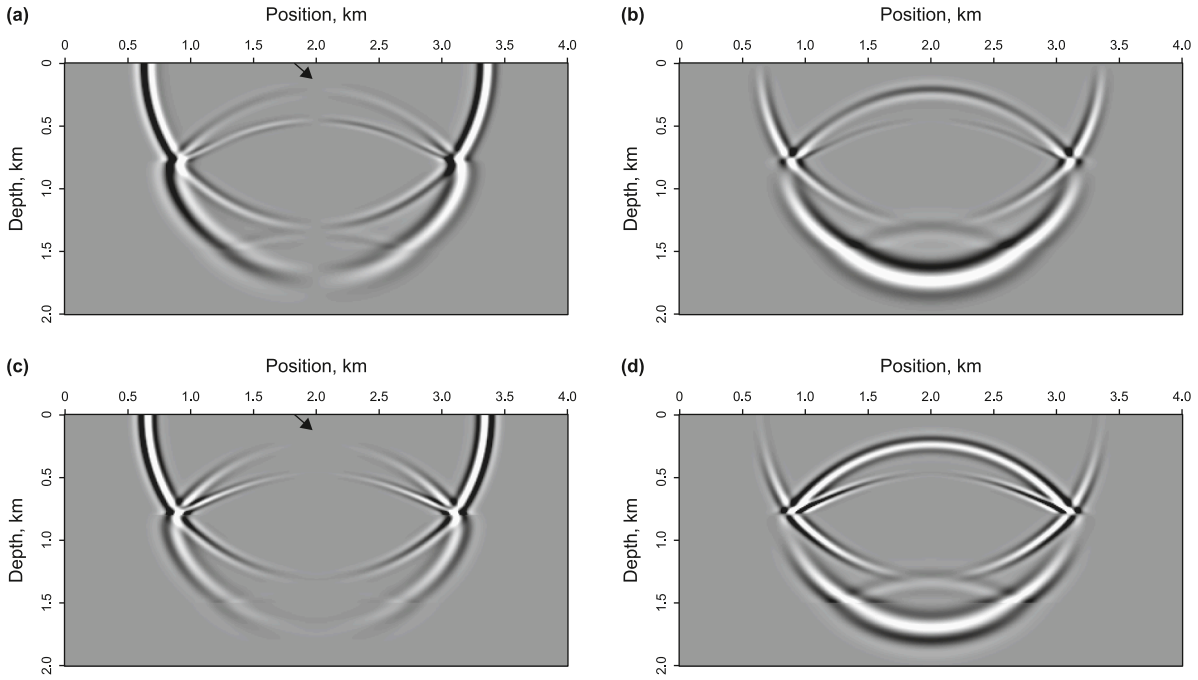

Fig. 5. Snapshots at 1.0 *s* for the layered model. Panels **(a)** and **(b)** show particle-velocity in *x*- and *z*-directions, respectively. Panels **(c)** and **(d)** show strain-rate in *x*- and *z*-directions, respectively.

$$
\begin{aligned}
\rho\frac{\partial \dot{\varepsilon}_{xx}}{\partial t} &= \frac{\partial^2\sigma_{xx}}{\partial x^2}+\frac{\partial^2\tau_{xx}}{\partial y^2}+\frac{\partial^2\tau_{yy}}{\partial x^2}+\frac{\partial^2\tau_{xx}}{\partial z^2}+\frac{\partial^2\tau_{zz}}{\partial x^2},\\
\rho\frac{\partial \dot{\varepsilon}_{yy}}{\partial t} &= \frac{\partial^2\sigma_{yy}}{\partial y^2}+\frac{\partial^2\tau_{xx}}{\partial y^2}+\frac{\partial^2\tau_{yy}}{\partial x^2}+\frac{\partial^2\tau_{yy}}{\partial z^2}+\frac{\partial^2\tau_{zz}}{\partial y^2},\\
\rho\frac{\partial \dot{\varepsilon}_{zz}}{\partial t} &= \frac{\partial^2\sigma_{zz}}{\partial z^2}+\frac{\partial^2\tau_{xx}}{\partial z^2}+\frac{\partial^2\tau_{zz}}{\partial x^2}+\frac{\partial^2\tau_{yy}}{\partial z^2}+\frac{\partial^2\tau_{zz}}{\partial y^2},\\
\frac{\partial\sigma_{xx}}{\partial t} &= (\lambda+2\mu)\dot{\varepsilon}_{xx}+\lambda\left(\dot{\varepsilon}_{yy}+\dot{\varepsilon}_{zz}\right),\\
\frac{\partial\sigma_{yy}}{\partial t} &= (\lambda+2\mu)\dot{\varepsilon}_{yy}+\lambda(\dot{\varepsilon}_{xx}+\dot{\varepsilon}_{zz}),\\
\frac{\partial\sigma_{zz}}{\partial t} &= (\lambda+2\mu)\dot{\varepsilon}_{zz}+\lambda\left(\dot{\varepsilon}_{xx}+\dot{\varepsilon}_{yy}\right),\\
\frac{\partial\tau_{xx}}{\partial t} &= \mu\dot{\varepsilon}_{xx},\\
\frac{\partial\tau_{yy}}{\partial t} &= \mu\dot{\varepsilon}_{yy},\\
\frac{\partial\tau_{zz}}{\partial t} &= \mu\dot{\varepsilon}_{zz},
\end{aligned}
\tag{9}
$$

where τ_{xx}, τ_{yy} and τ_{zz} are auxiliary variables. The normal strain-rate in each direction analogous to the response of a straight optical fiber along the same direction. Performing the Eq. (A.1), we compute the amplitude radiation patterns of different wavefields for a straight optical fiber, which reveal that the straight optical fiber is insensitive to normally incident seismic waves (Fig. 1).

The numerical solution of Eq. (9) employs the staggered-grid finite-difference scheme with eighth-order accuracy in space and second-order accuracy in time, along with the traditional CPML boundary conditions, and its stability conditions are satisfied

$$
\max(V_{\mathrm{p}})\Delta t\sqrt{\frac{1}{\Delta x^2}+\frac{1}{\Delta z^2}}\le 0.7774179, \tag{10}
$$

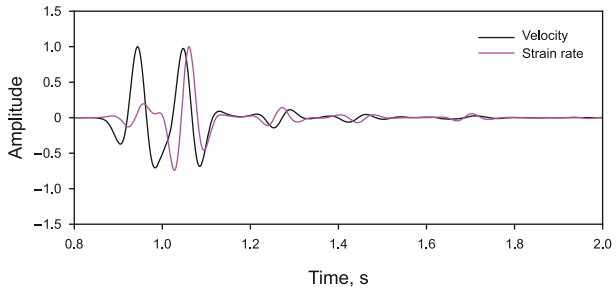

Fig. 6. Single-trace waveforms of *z*-component in the vertical well for the layered model. The black solid line denotes the particle-velocity, the magenta solid line denotes the strain-rate.

where the V_{p} is P-wave velocity, the Δt is time sampling interval, and Δx and Δz are spatial step in the x and z directions, respectively.

2.2. Seismic response with helical-wound optical fiber

The tangential strain-rate in the local coordinate system of a helical-wound optical fiber can be expressed as (Eaid et al., 2020)

$$
\begin{aligned}
\dot{\varepsilon}_{tt}(c) = {}& (\tilde{\mathbf{t}}\cdot\tilde{\mathbf{x}})^2\dot{\varepsilon}_{xx}+(\tilde{\mathbf{t}}\cdot\tilde{\mathbf{y}})^2\dot{\varepsilon}_{yy}+(\tilde{\mathbf{t}}\cdot\tilde{\mathbf{z}})^2\dot{\varepsilon}_{zz}\\
&+2(\tilde{\mathbf{t}}\cdot\tilde{\mathbf{x}})(\tilde{\mathbf{t}}\cdot\tilde{\mathbf{y}})\dot{\varepsilon}_{xy}+2(\tilde{\mathbf{t}}\cdot\tilde{\mathbf{x}})(\tilde{\mathbf{t}}\cdot\tilde{\mathbf{z}})\dot{\varepsilon}_{xz}+2(\tilde{\mathbf{t}}\cdot\tilde{\mathbf{y}})(\tilde{\mathbf{t}}\cdot\tilde{\mathbf{z}})\dot{\varepsilon}_{yz}
\end{aligned}
\tag{11}
$$

with

$$
\mathbf{T}(s)=\begin{bmatrix}
\tilde{\mathbf{t}}(c)\cdot\tilde{\mathbf{x}} & \tilde{\mathbf{t}}(c)\cdot\tilde{\mathbf{y}} & \tilde{\mathbf{t}}(c)\cdot\tilde{\mathbf{z}}\\
\tilde{\mathbf{n}}(c)\cdot\tilde{\mathbf{x}} & \tilde{\mathbf{n}}(c)\cdot\tilde{\mathbf{y}} & \tilde{\mathbf{n}}(c)\cdot\tilde{\mathbf{z}}\\
\tilde{\mathbf{b}}(c)\cdot\tilde{\mathbf{x}} & \tilde{\mathbf{b}}(c)\cdot\tilde{\mathbf{y}} & \tilde{\mathbf{b}}(c)\cdot\tilde{\mathbf{z}}
\end{bmatrix}, \tag{12}
$$

where the subscript *tt* represents tangential direction of the fiber, *c* denotes any point along the tangential direction, $\dot{\varepsilon}_{xx}$, $\dot{\varepsilon}_{yy}$ and $\dot{\varepsilon}_{zz}$ are

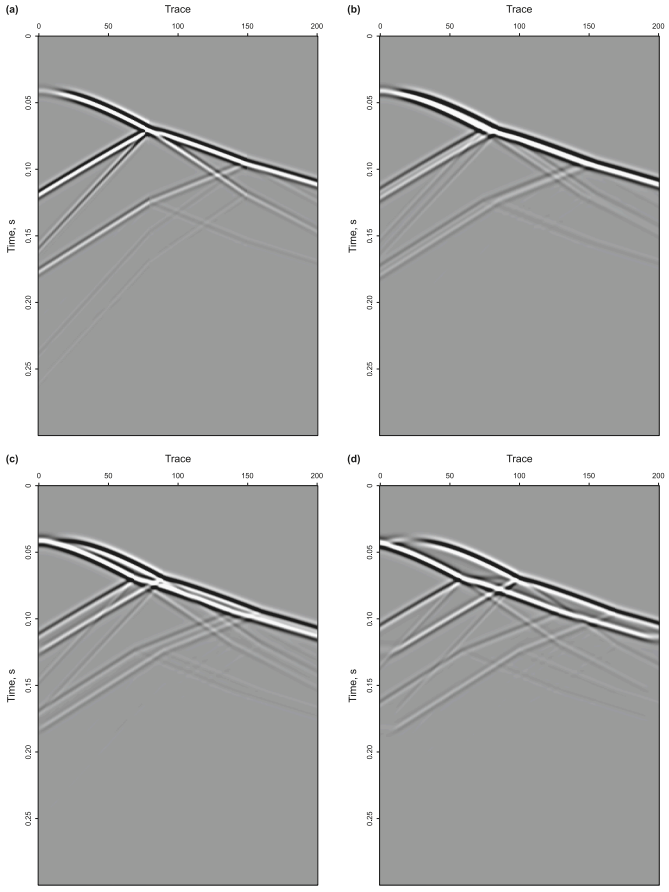

Fig. 7. Common-shot gathers of *z*-component in the vertical well with different gauge lengths for the layered model. Panel **(a)** shows the origin seismogram. Panel **(b)** shows the gauge length is 10 m. Panel **(c)** shows the gauge length is 20 m. Panel **(d)** shows the gauge length is 40 m.

the normal strain-rate components, $\dot{\varepsilon}_{xy}$, $\dot{\varepsilon}_{xz}$ and $\dot{\varepsilon}_{yz}$ are the shear strain-rate components, the unit vectors $\tilde{\mathbf{t}}(c)$ and its associated normal and binormal vectors $\tilde{\mathbf{n}}(c)$ and $\tilde{\mathbf{b}}(c)$ form the Frenet-Serret coordinate system, $\tilde{\mathbf{x}}$, $\tilde{\mathbf{y}}$, $\tilde{\mathbf{z}}$ represent the unit vectors of Cartesian coordinate system, $\mathbf{T}(c)$ is the rotation operator transforming between the Frenet-Serret coordinate system and the Cartesian coordinate system.

As mentioned by Eaid et al. (2020), a helical-wound optical fiber is insensitive to shear strain-rate components when it is symmetrical and periodic, and its axial strain-rate can be expressed as a weighted summation of normal strain-rate, where the sensitivity to each normal components is determined by the winding angle.

Assuming the winding core of a symmetrical and periodic helical fiber is aligned with the *x*-axis, this study investigates fibers with winding angles of 35.3° and 54.7°. For the 35.3°, the ratio between the normal strain-rate components is $\dot{\varepsilon}_{xx} : \dot{\varepsilon}_{yy} : \dot{\varepsilon}_{zz} = 1 : 1 : 1$, and its axial strain-rate can be computed as

$$\dot{\varepsilon}_{tt} = \dot{\varepsilon}_{xx} + \dot{\varepsilon}_{yy} + \dot{\varepsilon}_{zz}, \tag{13}$$

when the winding angle is 54.7°, the ratio between the normal strain-rate components is $\dot{\varepsilon}_{xx} : \dot{\varepsilon}_{yy} : \dot{\varepsilon}_{zz} = 4 : 1 : 1$, and its axial strain-rate can be calculated as

$$\dot{\varepsilon}_{tt} = 4\dot{\varepsilon}_{xx} + \dot{\varepsilon}_{yy} + \dot{\varepsilon}_{zz}. \tag{14}$$

Based on the Eqs. (A.2) and (A.3), we also plot the amplitude radiation patterns of different wavefields for helical-wound optical fibers at angles of 35.3° and 54.7° (Fig. 2). It indicates that the helical fiber at 35.3° is sensitive only to P-waves, whereas at 54.7°, it responds to S-waves.

2.3. Gauge length effects on optical fiber

DAS typically measures the average strain or strain-rate over a specified gauge length, which significantly influences the

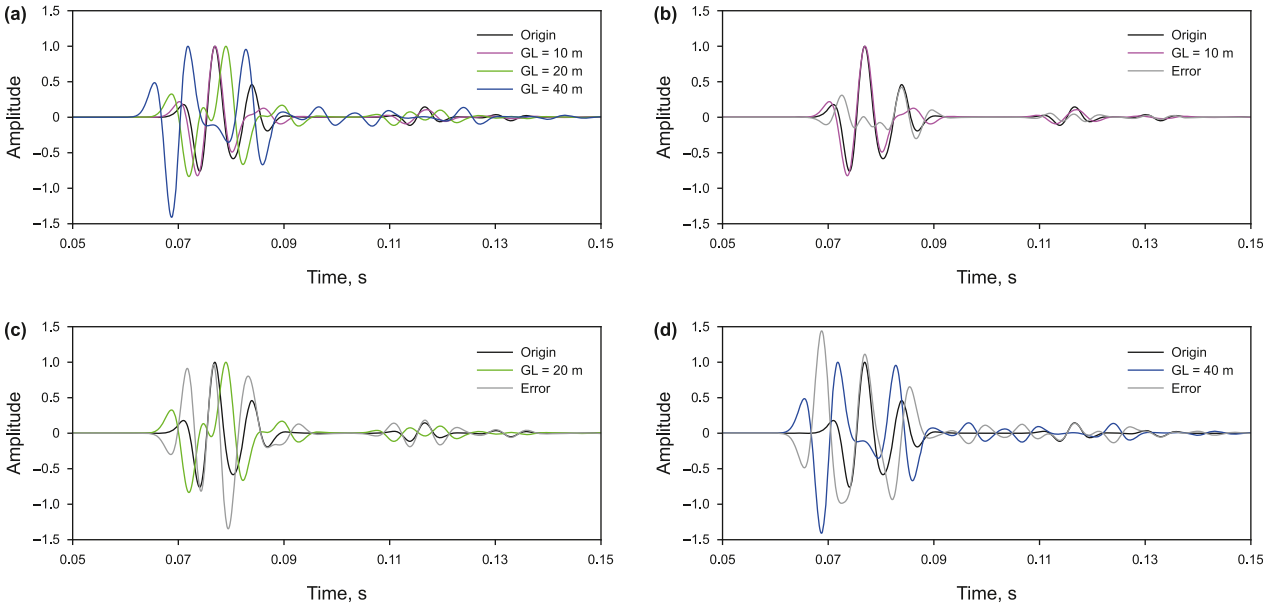

Fig. 8. Single-trace waveforms comparison of *z*-component strain-rate in the vertical well for the layer model. Panel **(a)** shows the different gauge lengths (GL). Panel **(b)** shows the comparison between origin and 10 m gauge length and their error curve. Panel **(c)** shows the comparison between origin and 20 m gauge length and their error curve. Panel **(d)** shows the comparison between origin and 40 m gauge length and their error curve. The black solid line denotes the original data, the magenta solid line denotes the gauge length is 10 m, the green solid line denotes the gauge length is 20 m, the blue solid line denotes the gauge length is 40 m, and the grey solid line denotes the error.

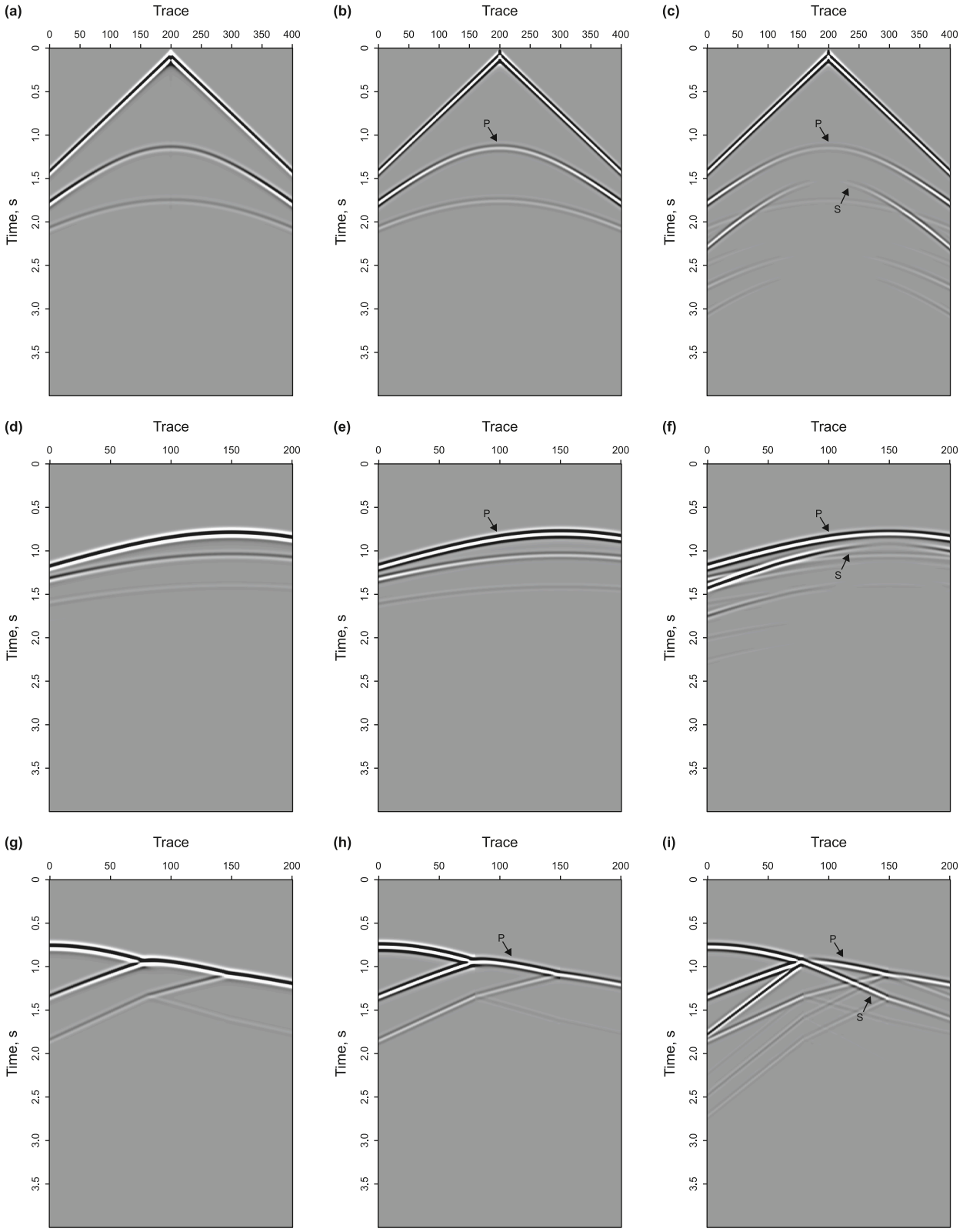

Fig. 9. Common-shot gathers of helical-wound optical fiber for the layered model. The first row displays receivers on the surface, panel **(a)** shows pressure seismogram, panels **(b)** and **(c)** show axial stain-rate seismogram at 35.3° and 54.7°, respectively. The second row displays receivers in the horizontal well, panel **(d)** shows pressure seismogram, panels **(e)** and **(f)** show axial stain-rate seismograms at 35.3° and 54.7°, respectively. The third row displays receivers in the vertical well, panel **(g)** shows pressure seismogram, panels **(h)** and **(i)** show stain-rate seismograms at 35.3° and 54.7°, respectively.

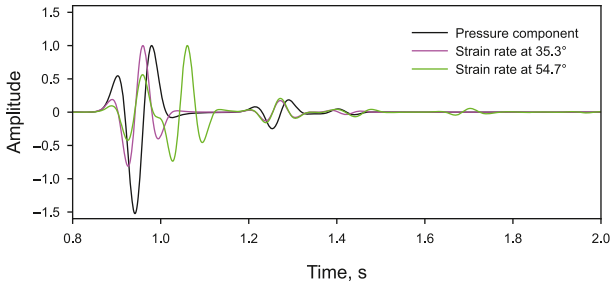

Fig. 10. Single-trace waveforms of helical-wound optical fiber in the vertical well for the layered model. The black solid line denotes the pressure, the magenta solid line denotes 35.3°, and the green solid line denotes 54.7°.

measurement accuracy (Daley et al., 2013; Dean et al., 2017). The strain-rate at position s with a gauge length L can be expressed as (Eaid et al., 2020; Zhang et al., 2024)

$$\dot{\varepsilon}_d(s) = \dot{\varepsilon}_{xx}G_{xx} + \dot{\varepsilon}_{yy}G_{yy} + \dot{\varepsilon}_{zz}G_{zz} + \dot{\varepsilon}_{xy}G_{xy} + \dot{\varepsilon}_{xz}G_{xz} + \dot{\varepsilon}_{yz}G_{yz}, \tag{15}$$

with

$$\begin{aligned}
G_{xx} &= \frac{1}{L}\int_{-L/2}^{+L/2} \tilde{t}_x(s')^2 \mathrm{d}s', \\
G_{yy} &= \frac{1}{L}\int_{-L/2}^{+L/2} \tilde{t}_y(s')^2 \mathrm{d}s', \\
G_{zz} &= \frac{1}{L}\int_{-L/2}^{+L/2} \tilde{t}_z(s')^2 \mathrm{d}s', \\
G_{xy} &= \frac{2}{L}\int_{-L/2}^{+L/2} \tilde{t}_x(s')\tilde{t}_y(s') \mathrm{d}s', \\
G_{xz} &= \frac{2}{L}\int_{-L/2}^{+L/2} \tilde{t}_x(s')\tilde{t}_z(s') \mathrm{d}s', \\
G_{yz} &= \frac{2}{L}\int_{-L/2}^{+L/2} \tilde{t}_y(s')\tilde{t}_z(s') \mathrm{d}s',
\end{aligned} \tag{16}$$

where L is the gauge length, $\tilde{t}_i(i = x, y, z)$ means the tangential direction, s' is the position of the sampling point in the fiber, G_{xx}, G_{yy} and G_{zz} are the fiber-dependent sensitivities to normal strain-rate components, G_{xy}, G_{yz} and G_{xz} are the fiber-dependent sensitivities to shear strain-rate components.

Eqs. (15) and (16) indicate that DAS measures the average strain-rate over the L length. Obviously, it smooths the DAS signal over the gauge length, which can enhance the signal-to-noise ratio but may lead to reduced measurement accuracy. Within the finite-difference framework, we average the strain-rate across multi grids to verify the effect of gauge length on DAS.

3. Numerical examples

In this chapter, we evaluate the proposed stress and strain-rate elastic equation using three 2D numerical models. Three geometries are designed, with receivers deployed on the surface, in a horizontal well, and in a vertical well, respectively. Our simulation employs the staggered-grid finite-difference scheme with eighth-order accuracy in space and second-order accuracy in time.

3.1. A layered model

The velocity models depicted in Fig. 3 consist of 201 × 401 grids with a spacing of 10 m in both x- and z-directions. The Ricker wavelet with a peak frequency of 10 Hz is employed as the explosive source-time function. The positions of source and receiver are illustrated within the V_p model, with the red star denotes the source location. A total of 401 traces on the surface represented by green dots, and 201 traces in the horizontal well shown as black dots, and 201 traces in the vertical well indicated by blue dots. Performing the first-order stress and strain-rate elastic wave equation to simulate the propagation of normal strain-rate wavefields. Taking the traditional velocity wavefields as the reference, we solve the stress-velocity elastic wave equation using the same simulation strategy.

Fig. 4 presents a comparison of x- and z-component common-shot gathers for particle-velocity and strain-rate in three geometries. Both events are comparable, including direct P-waves, reflected P-waves, reflected S-waves, and converted S-waves.

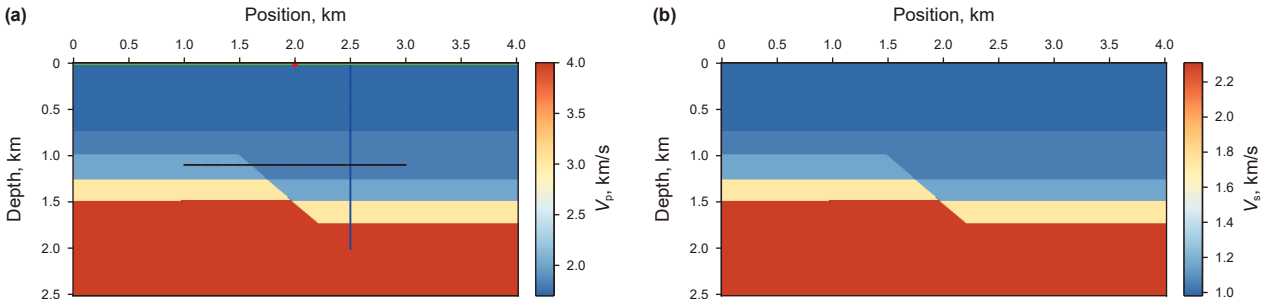

Fig. 11. The P- **(a)** and S-wave **(b)** velocities for the fault model. The red star denotes the source location, green dots denote receivers on the surface, black dots denote receivers in a horizontal well, and blue dots denote receivers in a vertical well.

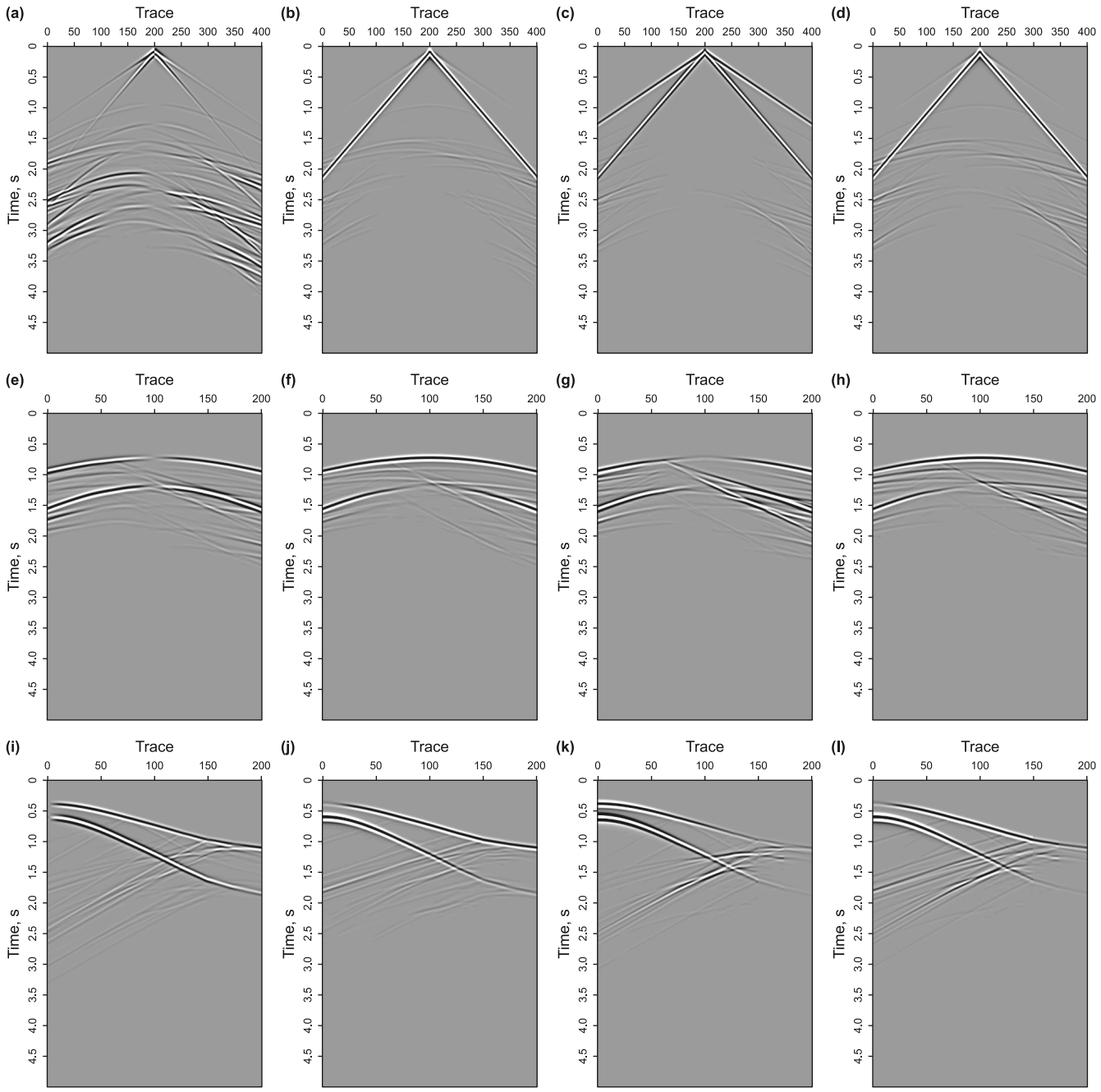

Fig. 12. Common-shot gathers for the fault model. The first row displays receivers on the surface, panels **(a)** and **(b)** show *x*- and *z*-component particle-velocity seismograms, and panels **(c)** and **(d)** show *x*- and *z*-component strain-rate seismograms. The second row displays receivers in the horizontal well, panels **(e)** and **(f)** show *x*- and *z*-component particle-velocity seismograms, panels **(g)** and **(h)** show *x*- and *z*-component strain-rate seismograms. The third row displays receivers in the vertical well, panels **(i)** and **(j)** show *x*- and *z*-component particle-velocity seismograms, and panels **(k)** and **(l)** show *x*- and *z*-component strain-rate seismograms.

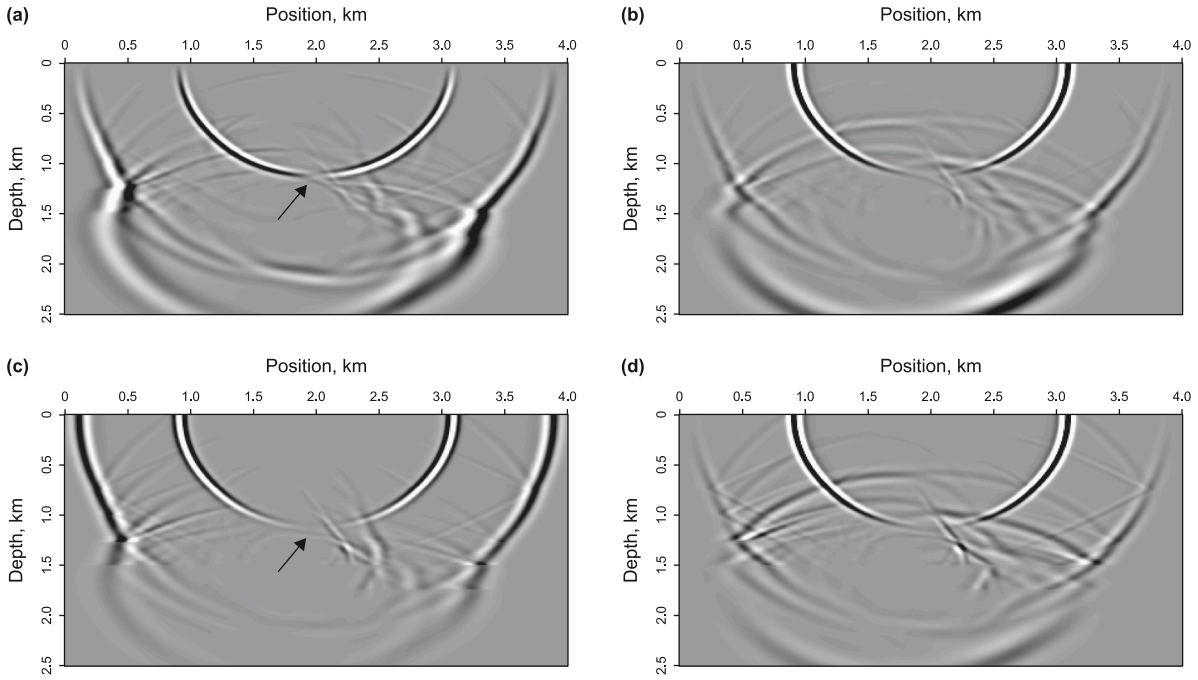

Fig. 13. Snapshots at 1.2 s for the fault model. Panels **(a)** and **(b)** show particle-velocity in *x*- and *z*-directions, respectively. Panels **(c)** and **(d)** show strain-rate in *x*- and *z*-directions, respectively.

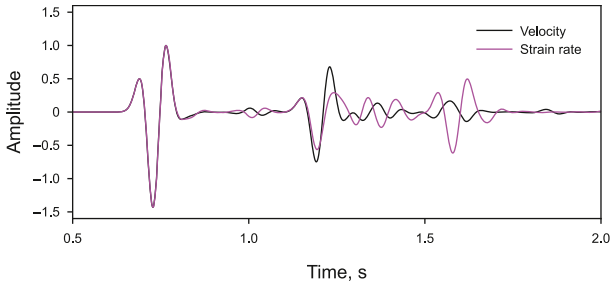

Fig. 14. Single-trace waveforms of *z*-component in the vertical well for the fault model. The black solid line denotes the particle-velocity, the magenta solid line denotes the strain-rate.

Compared to the particle-velocity (Fig. 4(a), (e)), the *x*-component strain-rate seismograms on the surface and in the horizontal well (Fig. 4(c), (g)) exhibit weak signals at near-offset due to the insensitivity to vertically incident waves on the fiber, while their *z*-component seismograms (Fig. 4(b), (f), (d), (h)) are similar. A comparison of seismograms in the vertical well for particle-velocity (Fig. 4(i) and (j)) and strain-rate (Fig. 4(k) and (l)) reveals minimal differences in wavefield types. The snapshots at 1.0 s in the *x*- and *z*-directions are illustrated in Fig. 5. Compared to the particle-velocity (Fig. 5(a) and (b)), the propagation of strain-rate wavefields (Fig. 5(c) and (d)) is correct, and the broadside insensitivity can also be clearly observed (indicated by black arrows). Detailed single-trace waveforms of the *z*-component seismograms in the vertical well are presented in Fig. 6. It can be seen that the differences of wavefield types between the particle-velocity and strain-rate are minimal.

We also calculate the average strain-rate over 11, 21 and 41 grids, which are equivalent to gauge lengths of 10, 20 and 40 m. The grid step of the simulation is 1 m, with a sampling interval of 0.1 ms and a duration of 0.3 s. The comparison of *z*-component seismograms in the vertical well is shown in Fig. 7, and their corresponding single-trace waveforms with different gauge lengths (Fig. 8(a)) and error curves (Fig. 8(b), (c), (d)) reveal that the measurement accuracy of DAS continuously decreases as the gauge length increases. Furthermore, we calculate the axial strain-rate of helical-wound optical fibers using the simulated normal strain-rate components. Fig. 9 compares the traditional pressure wavefields with axial strain-rate wavefields at winding angles of 35.3° and 54.7° in three geometries. It can be seen that the helical-wound optical fiber at 35.3° (Fig. 9(b)–(e), (h)) do not respond to S-waves (indicated by black arrows), similar to the pressure wavefields (Fig. 9(a)–(d), (g)). When the winding angle is adjusted to 54.7°, the S-waves can be accurately recorded (Fig. 9(c)–(f), (i), indicated by black arrows). These changes can also be observed in the detailed single-trace waveforms, exemplified by the data in the vertical well shown in Fig. 10.

3.2. A fault model

The fault model consists of 251 × 401 grids with a spacing of 10 m in both *x*- and *z*-directions. Fig. 11 shows the true P- and S-

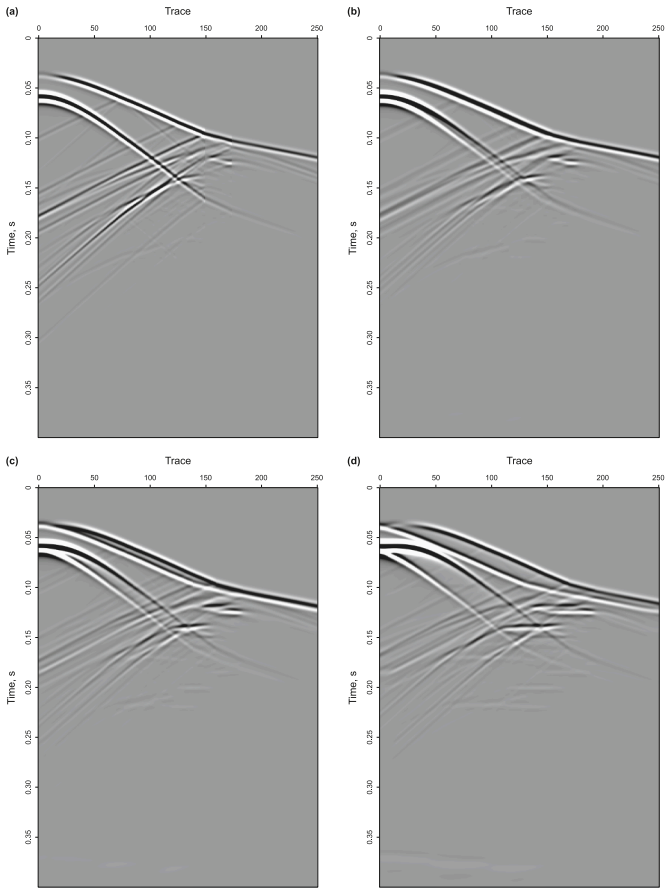

Fig. 15. Common-shot gathers of *z*-component in the vertical well with different gauge lengths for the fault model. Panel **(a)** shows the origin seismogram. Panel **(b)** shows the gauge length is 10 m. Panel **(c)** shows the gauge length is 20 m. Panel **(d)** shows the gauge length is 40 m.

wave velocity models. A Ricker wavelet with a peak frequency of 10 Hz is used as the vertical source function. Receivers are installed on the surface, in a horizontal well, and in a vertical well, represented by 401 green dots, 201 black dots, and 201 blue dots, as shown in the V_p model. To validate the accuracy of the presented equation, the staggered-grid finite-difference is employed to solve the first-order elastic wave equations of stress-strain-rate and stress-particle-velocity, followed by a comparison of the two wavefields.

In three geometries, the normal strain-rate wavefields are simulated and compared with the particle-velocity wavefields, as shown in Fig. 12. These wavefields reveal the presence of direct P-waves, direct S-waves, reflected P-waves, reflected S-waves, and converted waves, indicating the similarity in wavefield types. Due to the insensitivity to vertically incident waves, the strain-rate on the surface and in the horizontal well (Fig. 12(b)–(g)) exhibit weak signals at near-offset, which can be clearly observed from the snapshots (Fig. 13, indicated by black arrows). The single-trace waveforms (Fig. 14) provide further evidence that the proposed equation can generate accurate wavefields. Additionally, the strain-rate wavefields corresponding to gauge lengths of 10, 20 and 40 m are simulated with a spatial step size of 1m, a sampling interval of 0.08 ms, and a duration of 0.4 s. A comparison of the *z*-component shot gathers in the vertical well are shown in Fig. 15. The single-trace waveforms with different gauge lengths (Fig. 16(a)) and the error curve (Fig. 16(b), (c), (d)) indicate that the measurement accuracy of DAS decreases as the gauge length increases.

Furthermore, as shown in Fig. 17, the axial strain-rate wavefields of helical-wound optical fibers with winding angles of 35.3° and 54.7° are calculated under three geometries. For the winding angle of 35.3° (Fig. 17(b)–(e), (h)), the strain-rate seismograms demonstrate insensitivity to S-waves (indicated by black arrows), resembling conventional pressure components (Fig. 17(a)–(d), (g)). When the winding angle is 54.7° (Fig. 17(c)–(f), (i)), there are significant responses to S-waves (indicated by black arrows). This

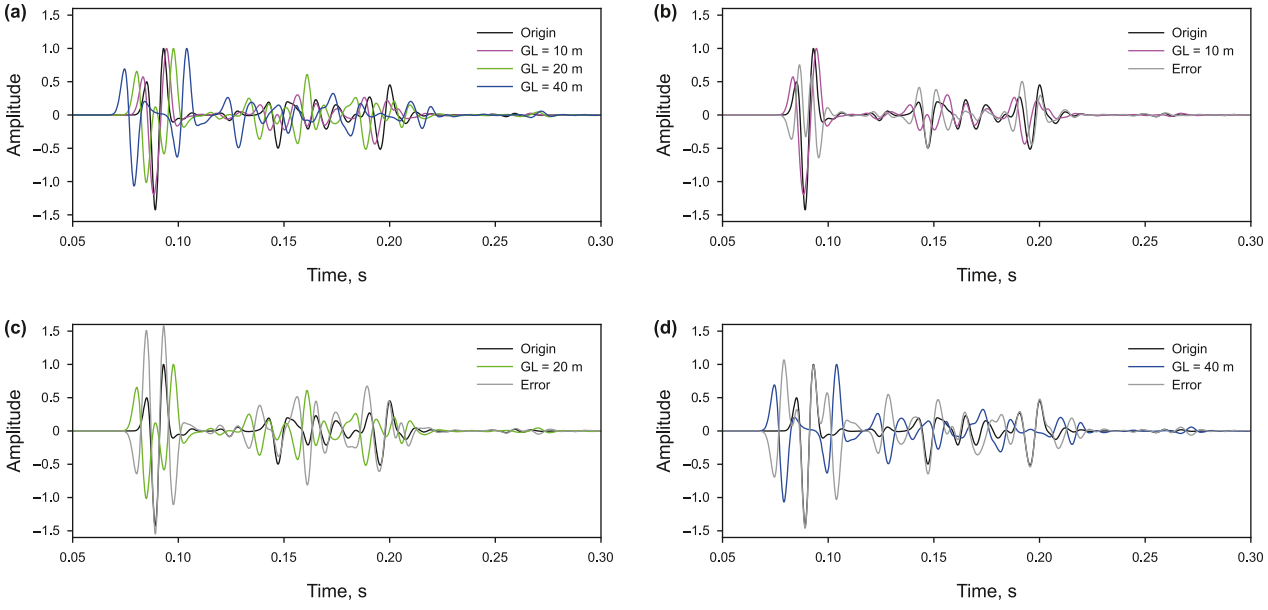

Fig. 16. Single-trace waveforms comparison of *z*-component strain-rate in the vertical well for the fault model. Panel **(a)** shows the different gauge lengths. Panel **(b)** shows the comparison between origin and 10 m gauge length and their error curve. Panel **(c)** shows the comparison between origin and 20 m gauge length and their error curve. Panel **(d)** shows the comparison between origin and 40 m gauge length and their error curve. The black solid line denotes the original data, the magenta solid line denotes the gauge length is 10 m, the green solid line denotes the gauge length is 20 m, the blue solid line denotes the gauge length is 40 m, and the grey solid line denotes the error.

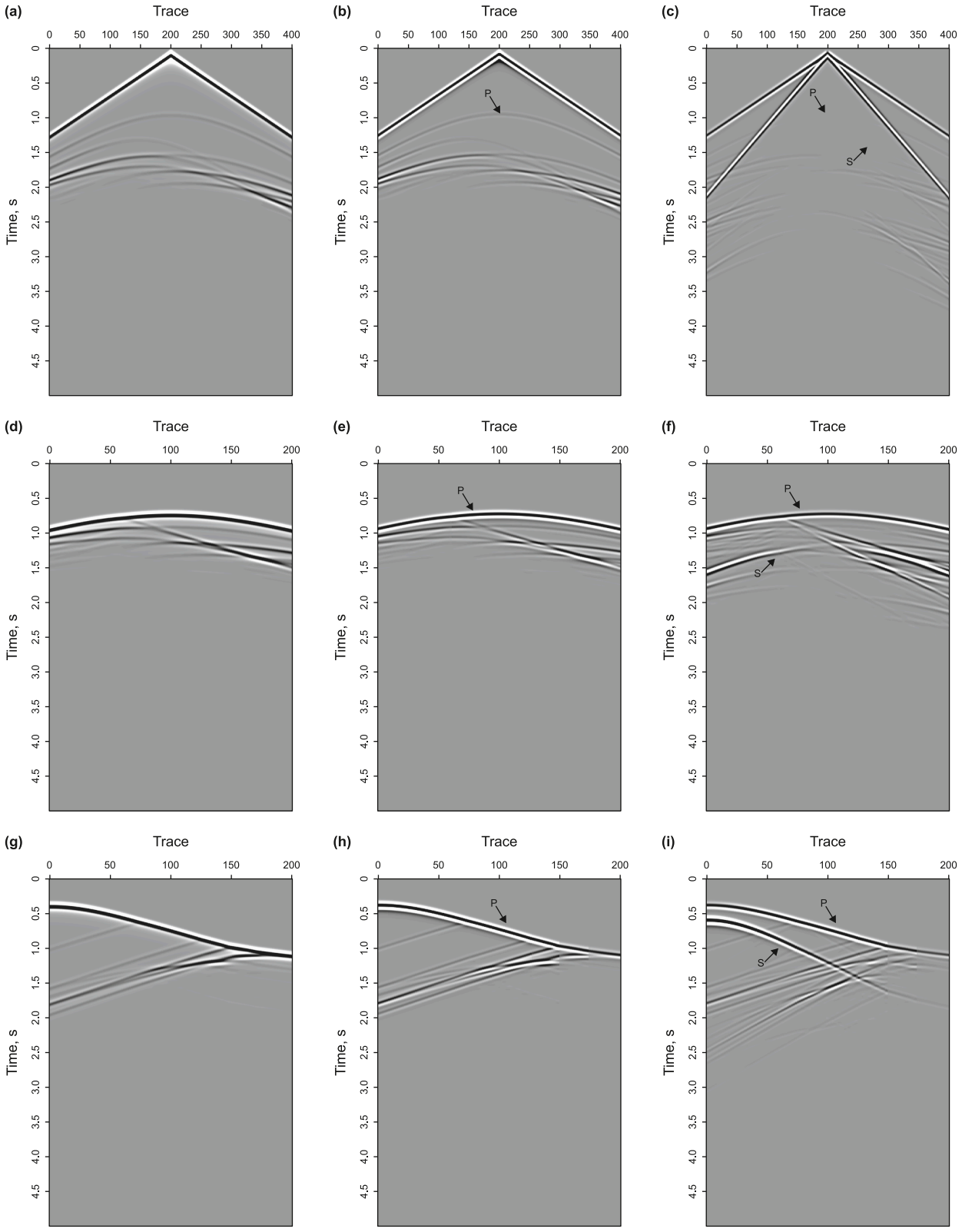

Fig. 17. Common-shot gathers of helical-wound optical fiber for the fault model. The first row displays receivers on the surface, panel **(a)** shows pressure seismogram, panels **(b)** and **(c)** show axial stain-rate seismogram at 35.3° and 54.7°, respectively. The second row displays receivers in the horizontal well, panel **(d)** shows pressure seismogram, panels **(e)** and **(f)** show axial stain-rate seismograms at 35.3° and 54.7°, respectively. The third row displays receivers in the vertical well, panel **(g)** shows pressure seismogram, panels **(h)** and **(i)** show axial stain-rate seismograms at 35.3° and 54.7°, respectively.

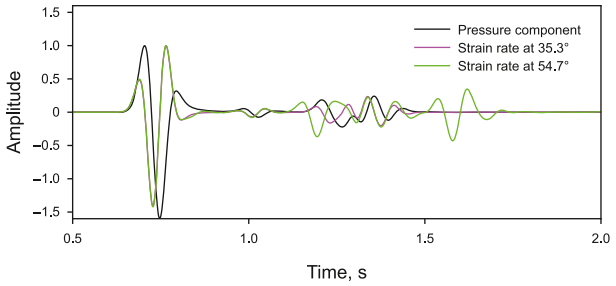

Fig. 18. Single-trace waveforms of helical-wound optical fiber in the vertical well for the fault model. The black solid line denotes the pressure, the magenta solid line denotes axial strain-rate at winding angle of 35.3°, and the green solid line denotes axial strain-rate at winding angle of 54.7°.

distinction is further evidenced by single-trace waveforms comparison in Fig. 18.

3.3. The Marmousi model

The third example is the Marmousi model, displayed in Fig. 19. Fig. 19(b) is the S-wave velocity, derived by multiplying the P-wave velocity (Fig. 19(a)) by 0.58. The density remains constant at 2.0 g/cm^3. The model consists of 264 × 1701 grids with a spatial step size of 10 m. A Ricker wavelet with a peak frequency of 12 Hz is used as the explosive source function. The recording duration time totals 6 s, featuring a time sampling interval of 1 ms. The number of traces for the surface, horizontal well, and vertical well are 601,

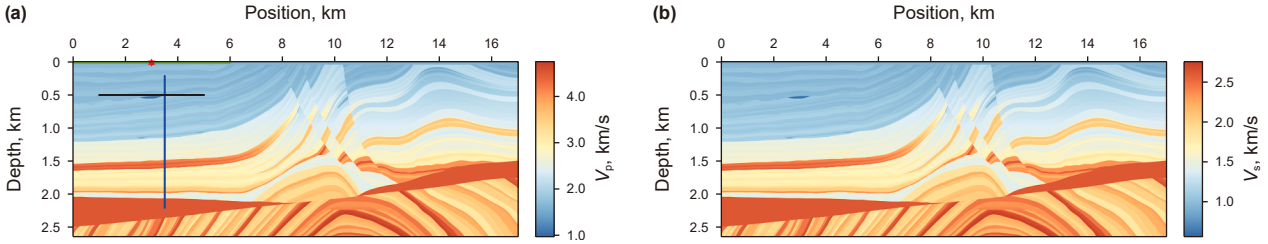

Fig. 19. The P- **(a)** and S-wave **(b)** velocities for the Marmousi model. The red star denotes the source location, green dots denote receivers on the surface, black dots denote receivers in a horizontal well, and blue dots denote receivers in a vertical well.

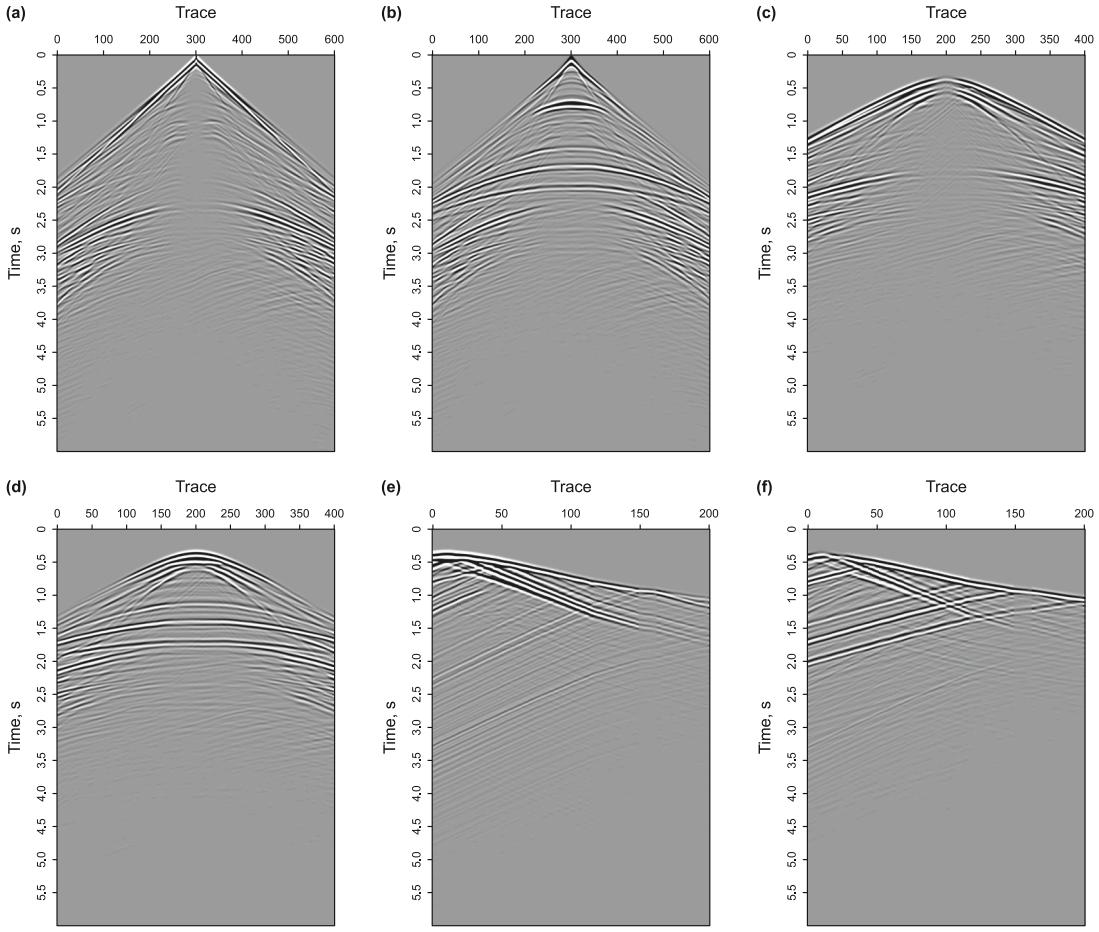

Fig. 20. Common-shot gathers for the Marmousi model. The first row displays receivers on the surface, panels **(a)** and **(b)** show *x*- and *z*-component strain-rate seismograms, respectively. The second row displays receivers in the horizontal well, panels **(c)** and **(d)** show *x*- and *z*-component strain-rate seismograms, respectively. The third row displays receivers in the vertical well, panels **(e)** and **(f)** show *x*- and *z*-component strain-rate seismograms, respectively.

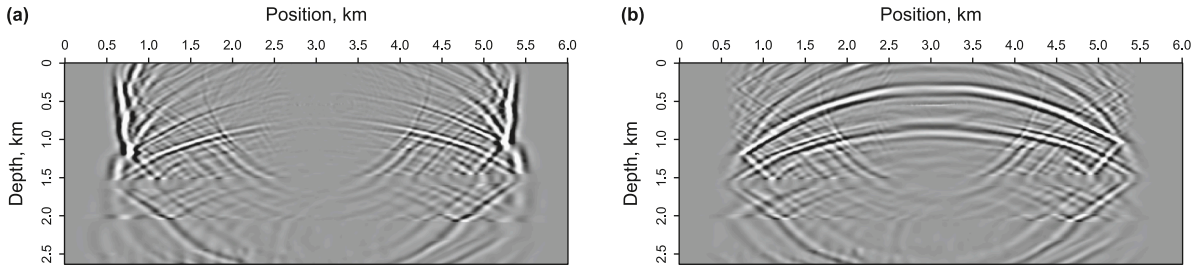

Fig. 21. Snapshots at 1.5 s for the Marmousi model. Panels **(a)** and **(b)** show the propagation of strain-rate wavefields in *x*- and *z*-directions, respectively.

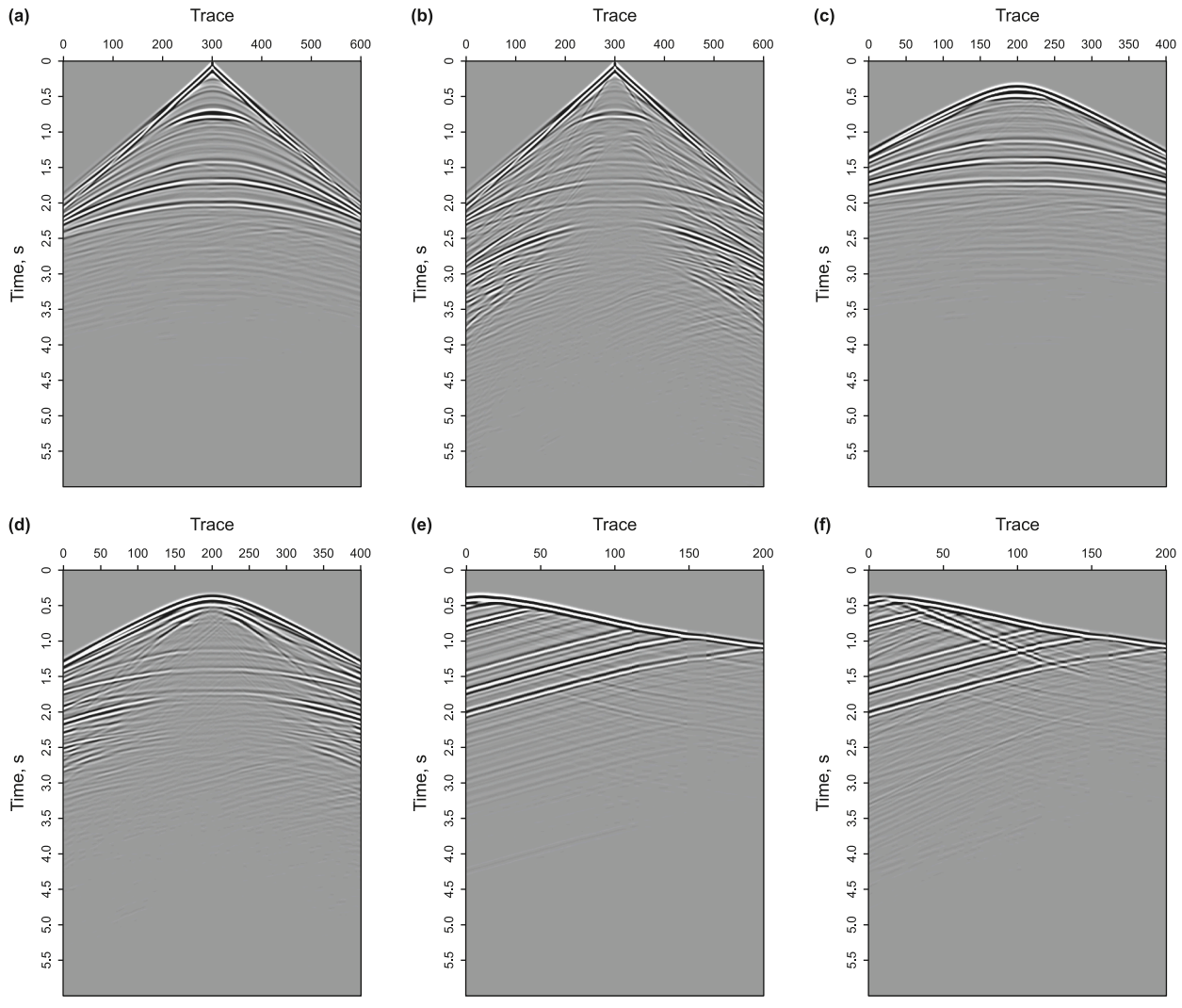

Fig. 22. Common-shot gathers of helical-wound optical fiber for the Marmousi model. The first row displays receivers on the surface, panels **(a)** and **(b)** show axial stain-rate seismograms at 35.3° and 54.7°, respectively. The second row displays receivers in the horizontal well, panels **(c)** and **(d)** show axial stain-rate seismograms at 35.3° and 54.7°, respectively. The third row displays receivers in the vertical well, panels **(e)** and **(f)** display axial stain-rate seismograms at 35.3° and 54.7°, respectively.

401, and 201, respectively, represented by green, black, and blue dots in the *Vp* model.

The strain-rate wavefields in *x*- and *z*-directions are simulated in three geometries (Fig. 20). These wavefields accurately capture direct P-waves, converted S-waves, reflected P-waves, and reflected S-waves. Fig. 21 presents snapshots at 1.5 s, demonstrating the accuracy of wavefield propagation and the broadside insensitivity of strain-rate. The axial strain-rate for helical-wound optical fibers are further calculated using the normal components. At a winding angle of 35.3°, the strain-rate records lack S-waves (Fig. 22(a)–(c), (e)). When the winding angle is 54.7°, there is a significant S-wave response in the seismic records (Fig. 22(b)–(d), (f)).

4. Discussion

The proposed novel first-order stress and strain-rate elastic wave equation is used to investigate the seismic response of multi-component DAS system. This equation recharacterizes the traditional first-order stress-velocity wave equation using stress and strain-rate, which is logical and mathematical. Three typical numerical models with different geometries and modeling parameters verify that the equation can accurately simulate the normal strain-rate wavefields and directly output multi-component DAS records without numerical dispersion or instability. However, validation with real data is not feasible due to a lack of multi-component field datasets.

DAS measures the average strain-rate over a specific gauge length, and an appropriate gauge length can balance measurement accuracy and signal-to-noise ratio of DAS. For the regular helical-wound fiber, varying winding angles can affect the sensitivity of normal strain-rate components in different directions. Therefore, suitable angles should be selected based on specific geological conditions. The proposed equation neglects shear strain-rate components, which may lead to inaccuracies in certain geological structures. When the helical-wound fiber is irregular, the contribution of shear components also needs to be considered.

Straight optical fiber exhibits broadside insensitivity and only contains single-component data. In contrast, helical-wound optical fiber can capture seismic response in multiple tangential directions, making it suitable for complex DAS seismic imaging or FWI. In traditional DAS seismic imaging or FWI, the initial step involves converting strain or strain-rate into displacement or particle-velocity, which can result in inaccurate results. To avoid this data conversion, the stress and strain-rate equation can be further directly implemented in multi-component DAS RTM or FWI.

5. Conclusion

To investigate the seismic response of multi-component DAS system, this study proposes a novel first-order stress and strain-rate elastic wave equation. This equation can produce the elastic normal strain-rate wavefields and directly output multi-component DAS data. By performing varying modeling parameters, such as refinement of grid and time step, this equation can still reliably simulate the propagation of strain-rate wavefields. The gauge length significantly affects the measurement accuracy of DAS, specifically, with large gauge length resulting in low measurement accuracy. The helical-wound optical fiber with a winding angle of 35.3° is sensitivity only to P-waves, similar to traditional pressure component, whereas the 54.7° can clearly record S-waves. Based on this equation, we can further develop multi-component DAS RTM or FWI that does not require data conversion.

CRediT authorship contribution statement

Chong Zhao: Writing – review & editing, Writing – original draft, Visualization, Validation, Supervision, Software, Resources, Project administration, Methodology, Investigation, Funding acquisition, Formal analysis, Data curation, Conceptualization. **Ji-Dong Yang:** Conceptualization. **Jian-Ping Huang:** Conceptualization. **Ning Qin:** Conceptualization. **Kun Tian:** Conceptuaization. **Fei-Long Yang:** Conceptualization.

Declaration of competing interest

The authors declare that they have no conflicts of interest with the contents of this article.

Appendix

The radiation patterns of wavefields for both straight and helical-wound optical fibers are given by the following expressions (Martin et al., 2018):

$$\begin{aligned}\dot{\varepsilon}^{S}_{\theta,P} = k^2 cA\Big(&\cos^2\theta_1\cos^2\theta_2\cos^2\varphi_1\cos^2\varphi_2+\\ &\frac{1}{2}\sin 2\theta_1\cos^2\theta_2\sin 2\varphi_1\cos^2\varphi_2-\\ &\frac{1}{2}\cos\theta_1\sin 2\theta_2\cos\varphi_1\sin 2\varphi_2+\\ &\sin^2\theta_1\cos^2\theta_2\sin^2\varphi_1\cos^2\varphi_2-\\ &\frac{1}{2}\sin\theta_1\sin 2\theta_2\sin\varphi_1\sin 2\varphi_2+\sin^2\theta_2\sin^2\varphi_2\Big)O,\\ \dot{\varepsilon}^{S}_{\theta,SV} = \frac{k^2 cA}{2}\Big(&-\cos^2\theta_1\cos^2\theta_2\cos^2\varphi_1\sin 2\varphi_2-\\ &\frac{1}{2}\sin 2\theta_1\cos^2\theta_2\sin 2\varphi_1\sin 2\varphi_2-\\ &\cos\theta_1\sin 2\theta_2\cos\varphi_1\cos 2\varphi_2-\\ &\sin^2\theta_1\cos^2\theta_2\sin^2\varphi_1\sin 2\varphi_2-\\ &\sin\theta_1\sin 2\theta_2\sin\varphi_1\cos 2\varphi_2+\sin^2\theta_2\sin 2\varphi_2\Big)O,\\ \dot{\varepsilon}^{S}_{\theta,SH} = \frac{k^2 cA}{2}\Big(&\cos^2\theta_1\cos^2\theta_2\sin 2\varphi_1\cos\varphi_2-\\ &\sin 2\theta_1\cos^2\theta_2\cos 2\varphi_1\cos\varphi_2-\\ &\cos\theta_1\sin 2\theta_2\sin\varphi_1\sin\varphi_2-\\ &\sin^2\theta_1\cos^2\theta_2\sin 2\varphi_1\cos\varphi_2+\\ &\sin\theta_1\sin 2\theta_2\cos\varphi_1\sin\varphi_2)O\end{aligned} \tag{A.1}$$

$$\dot{\varepsilon}^{35.3^\circ}_{\theta,P} = k^2 cAO, \dot{\varepsilon}^{35.3^\circ}_{\theta,SV} = 0, \dot{\varepsilon}^{35.3^\circ}_{\theta,SH} = 0 \tag{A.2}$$

$$\dot{\varepsilon}_{\theta,\mathrm{P}}^{54.7^\circ} = k^2 cA\Big(3\cos^2\theta_1\cos^2\theta_2\cos^2\varphi_1\cos^2\varphi_2+ \frac{3}{2}\sin 2\theta_1\cos^2\theta_2\sin 2\varphi_1\cos^2\varphi_2- \frac{3}{2}\cos\theta_1\sin 2\theta_2\cos\varphi_1\sin 2\varphi_2+ 3\sin^2\theta_1\cos^2\theta_2\sin^2\varphi_1\cos^2\varphi_2- \frac{3}{2}\sin\theta_1\sin 2\theta_2\sin\varphi_1\sin 2\varphi_2+3\sin^2\theta_2\sin^2\varphi_2+1\Big)O,$$

$$\dot{\varepsilon}_{\theta,\mathrm{SV}}^{54.7^\circ} = \frac{k^2 cA}{2}\Big(-3\cos^2\theta_1\cos^2\theta_2\cos^2\varphi_1\sin 2\varphi_2+ \frac{3}{2}\sin 2\theta_1\cos^2\theta_2\sin 2\varphi_1\sin 2\varphi_2- 3\cos\theta_1\sin 2\theta_2\cos\varphi_1\cos 2\varphi_2+ 3\sin^2\theta_1\cos^2\theta_2\sin^2\varphi_1\sin 2\varphi_2- 3\sin\theta_1\sin 2\theta_2\sin\varphi_1\cos 2\varphi_2+3\sin^2\theta_2\sin 2\varphi_2\Big)O,$$

$$\dot{\varepsilon}_{\theta,\mathrm{SH}}^{54.7^\circ} = \frac{k^2 cA}{2}\Big(3\cos^2\theta_1\cos^2\theta_2\sin 2\varphi_1\cos\varphi_2- 3\sin 2\theta_1\cos^2\theta_2\cos 2\varphi_1\cos\varphi_2- 3\cos\theta_1\sin 2\theta_2\sin\varphi_1\sin\varphi_2- 3\sin^2\theta_1\cos^2\theta_2\sin 2\varphi_1\cos\varphi_2+ 3\sin\theta_1\sin 2\theta_2\cos\varphi_1\sin\varphi_2)O \tag{A.3}$$

where $\dot{\varepsilon}_{\theta,\mathrm{P}}^{S}$, $\dot{\varepsilon}_{\theta,\mathrm{SV}}^{S}$, $\dot{\varepsilon}_{\theta,\mathrm{SH}}^{S}$ represent the P-wave, SV-wave, and SH-wave of straight optical fiber, respectively. $\dot{\varepsilon}_{\theta,\mathrm{P}}^{35.3^\circ}$, $\dot{\varepsilon}_{\theta,\mathrm{SV}}^{35.3^\circ}$, $\dot{\varepsilon}_{\theta,\mathrm{SH}}^{35.3^\circ}$ represent the P-wave, SV-wave, and SH-wave of helical-wound optical fiber with 35.3°, respectively. $\dot{\varepsilon}_{\theta,\mathrm{P}}^{54.7^\circ}$, $\dot{\varepsilon}_{\theta,\mathrm{SV}}^{54.7^\circ}$, $\dot{\varepsilon}_{\theta,\mathrm{SH}}^{54.7^\circ}$ represent the P-wave, SV-wave, and SH-wave of helical-wound optical fiber with 54.7°, respectively. The $(\cos\varphi_1\cos\varphi_2, \sin\varphi_1\cos\varphi_2, \sin\varphi_2)$ and $(\cos\theta_1\cos\theta_2, \sin\theta_1\cos\theta_2, \sin\theta_2)$ represent the propagation direction of seismic waves and the deployment orientation of DAS, respectively. φ_1 and φ_2 denote the angles of the seismic wave propagation direction relative to the x-axis and the xOy plane, respectively, whereas θ_1 and θ_2 represent the corresponding angles for the fiber orientation. k is wavenumber, $O = e^{ik(ct - x\cos\varphi_1\cos\varphi_2 - y\sin\varphi_1\cos\varphi_2 - z\sin\varphi_2)}$ is factor of body wave, c is phase velocity, and A is amplitude, x, y, z are coordinates, t is time.

References

Bakulin, A., Golikov, P., Smith, R., et al., 2017. Smart DAS upholes for simultaneous land near-surface characterization and subsurface imaging. Lead. Edge 36 (12), 1001–1008. https://doi.org/10.1190/tle36121001.1.

Bakulin, A., Silvestrov, I., Pevzner, R., 2020. Surface seismics with DAS: An emerging alternative to modern point-sensor acquisition. Lead. Edge 39 (11), 808–818. https://doi.org/10.1190/tle39110808.1A.

Byerley, G., Monk, D., Aaron, P., et al., 2018. Time-lapse seismic monitoring of individual hydraulic frac stages using a downhole DAS array. Lead. Edge 37 (11), 802–810. https://doi.org/10.1190/tle37110802.1.

Celli, N.L., Bean, C.J., O'Brien, G.S., 2024. Full-waveform simulation of DAS records, response and cable-ground coupling. Geophys. J. Int. 236 (1), 659–674. https://doi.org/10.1093/gji/ggad449.

Daley, T.M., Freifeld, B.M., Ajo-Franklin, J., et al., 2013. Field testing of fiber-optic distributed acoustic sensing (DAS) for subsurface seismic monitoring. Lead. Edge 32 (6), 699–706. https://doi.org/10.1190/tle32060699.1.

Dean, T., Cuny, T., Hartog, A.H., 2017. The effect of gauge length on axially incident P-waves measured using fibre optic distributed vibration sensing. Geophys. Prospect. 65 (1), 184–193. https://doi.org/10.1111/1365-2478.12419.

Dou, S., Ajo-Franklin, J., Daley, T., et al., 2016. Surface Orbital Vibrator (SOV) and fiber-optic DAS: Field Demonstration of Economical, continuous-land Seismic time-lapse Monitoring from the Australian CO2CRC Otway site. In: SEG International Exposition and Annual Meeting. SEG. SEG-2016-13974161.

Dou, S., Lindsey, N., Wagner, A.M., et al., 2017. Distributed acoustic sensing for seismic monitoring of the near surface: a traffic-noise interferometry case study. Sci. Rep. 7 (1), 11620. https://doi.org/10.1038/s41598-017-11986-4.

Eaid, M., Li, J., Innanen, K.A., 2018. Modeling the Response of shaped-DAS Fibres to Microseismic Moment Tensor sources. In: SEG International Exposition and Annual Meeting. SEG. https://doi.org/10.1190/segam2018-2998378.1.

Eaid, M.V., Keating, S.D., Innanen, K.A., 2020. Multiparameter seismic elastic full-waveform inversion with combined geophone and shaped fiber-optic cable data. Geophysics 85 (6), R537–R552. https://doi.org/10.1190/geo2020-0170.1.

Hall, K.W., Bertram, K.L., Bertram, M., et al., 2019. Simultaneous accelerometer and optical fibre multi-azimuth walk-away VSP experiment: Newell County, Alberta, Canada. In: SEG International Exposition and Annual Meeting. SEG,. https://doi.org/10.1190/segam2019-3216606.1.

Harris, K., White, D., Melanson, D., et al., 2016. Feasibility of time-lapse VSP monitoring at the aquistore CO_2 storage site using a distributed acoustic sensing system. Int. J. Greenh. Gas Control 50, 248–260. https://doi.org/10.1016/j.ijggc.2016.04.016.

Hendi, S., Gorjian, M., Bellefleur, G., et al., 2020. Investigation of the effects of surrounding media on the distributed acoustic sensing of helically-wound fiber-optic cable with application to the new afton deposit, British Columbia. Solid Earth Discussions 2020, 1–31. https://doi.org/10.5194/se-14-89-2023.

Hornman, J.C., 2017. Field trial of seismic recording using distributed acoustic sensing with broadside sensitive fibre-optic cables. Geophys. Prospect. 65 (1), 35–46. https://doi.org/10.1111/1365-2478.12358.

Innanen, K., 2017. Determination of seismic-tensor strain from helical wound cable-distributed acoustic sensing cable with arbitrary and nested-helix winds. SEG International Exposition and Annual Meeting. SEG. SEG-2017-17664060.

Kislov, K.V., Gravirov, V.V., 2022. Distributed acoustic sensing: A new tool or a new paradigm. Seism. Instrum. 58 (5), 485–508. https://doi.org/10.3103/S0747923922050085.

Kuvshinov, B.N., 2016. Interaction of helically wound fibre-optic cables with plane seismic waves. Geophys. Prospect. 64 (3), 671–688. https://doi.org/10.1111/1365-2478.12303.

Li, Y., Karrenbach, Martin, Ajo-Franklin, Jonathan (Eds.), 2022. Distributed Acoustic Sensing in Geophysics: Methods and Applications. John Wiley & Sons.

Lumens, P., Franzen, A., Hornman, K., et al., 2013. Cable development for distributed geophysical sensing with a field trial in surface seismic. Fifth European Workshop on Optical Fibre Sensors. SPIE 8794, 497–501. https://doi.org/10.1117/12.2025693.

Ma, G.Q., Cao, D.P., Yin, J.J., et al., 2020. Numerical simulation of detecting seismic signals in DAS wells. Oil Geophys. Prospect. 50, 311–320. https://doi.org/10.13810/j.cnki.issn.1000-7210.2020.02.012 (in Chinese).

Madsen, K.N., Thompson, M., Parker, T., et al., 2013. A VSP field trial using distributed acoustic sensing in a producing well in the North sea. First Break 31 (11). https://doi.org/10.3997/1365-2397.2013027.

Martin, E.R., Huot, F., Ma, Y., et al., 2018. A seismic shift in scalable acquisition demands new processing: Fiber-optic seismic signal retrieval in urban areas with unsupervised learning for coherent noise removal. IEEE Signal Process. Mag. 35 (2), 31–40. https://doi.org/10.1109/MSP.2017.2783381.

Masoudi, A., Belal, M., Newson, T.P., 2013. A distributed optical fibre dynamic strain sensor based on phase-OTDR. Meas. Sci. Technol. 24 (8), 085204. https://doi.org/10.1088/0957-0233/24/8/085204.

Mateeva, A., Lopez, J., Mestayer, J., et al., 2013. Distributed acoustic sensing for reservoir monitoring with VSP. Lead. Edge 32 (10), 1278–1283. https://doi.org/10.1190/tle32101278.1.

Ning, I.L.C., Sava, P., 2018a. Multicomponent distributed acoustic sensing: Concept and theory. Geophysics 83 (2), P1–P8. https://doi.org/10.1190/geo2017-0327.1.

Ning, I.L.C., Sava, P., 2018b. High-resolution multi-component distributed acoustic sensing. Geophys. Prospect. 66 (6), 1111–1122. https://doi.org/10.1111/1365-2478.12634.

Posey, Jr R., Johnson, G.A., Vohra, S.T., 2000. Strain sensing based on coherent Rayleigh scattering in an optical fibre. Electron. Lett. 36 (20), 1688–1689. https://doi.org/10.1049/el:20001200.

Shi, Z.W., Yang, J.D., Wang, Y.Z., et al., 2024. Three-dimensional seismic response mechanism of straight and helically wound optical fibers. Oil Geophys. Prospect. 59 (1), 80–88. https://doi.org/10.13810/j.cnki.issn.1000-7210.2024.01.009 (in Chinese).

Staněk, F., Jin, G., Simmons, J., 2022. Fracture imaging using DAS-recorded microseismic events. Front. Earth Sci. 10, 907749. https://doi.org/10.3389/feart.2022.907749.

Stork, A.L., Baird, A.F., Horne, S.A., et al., 2020. Application of machine learning to microseismic event detection in distributed acoustic sensing data. Geophysics 85 (5), KS149–KS160. https://doi.org/10.1190/geo2019-0774.1.

Virieux, J., 1986. P-SV wave propagation in heterogeneous media: Velocity-stress finite-difference method. Geophysics 51 (4), 889–901. https://doi.org/10.1190/1.1442147.

Willis, M.E.. Distributed Acoustic Sensing for Seismic measurements–what Geophysicists and Engineers Need to Know. Society of Exploration Geophysicists. https://doi.org/10.1190/1.9781560803850.

Zhang, L., Zhao, Y., Liu, L., et al., 2024. Strain field reconstruction from helical-winding fiber distributed acoustic sensing and its application in anisotropic elastic reverse time migration. Geophysics 89 (3), S251–S265. https://doi.org/10.1190/geo2023-0354.1.